FINAL REPORT

Analysis of Ozone Production Data from the San Antonio Field Study

AQRP Project 19-040

Prepared for:
Elena MacDonald-Buller
Texas Air Quality Research Program
The University of Texas at Austin

Prepared by:
Ezra Wood (Principal Investigator)
Department of Chemistry
Drexel University

Shannon Capps (Co-investigator)
Department of Civil, Architectural, and Environmental Engineering
Drexel University

September 2019

QA Requirements: Audits of Data Quality: 10% Required

Executive Summary

During May 2017, research groups from Drexel University, Aerodyne Research, University of Houston, Rice University, Baylor University, and others participated in the "San Antonio Field Study" with the overall goal of characterizing ozone formation in the greater San Antonio area. The Drexel team made measurements of total peroxy radicals ($[HO_2]$ + $[RO_2]$, "[ROx]") aboard the Aerodyne Mobile Laboratory at three sites upwind and downwind of San Antonio: at the University of Texas-San Antonio, which is in the Northwest of San Antonio, Floresville (Southeast of San Antonio), and Corpus Christi (Southeast of San Antonio). Combined with measurements of NO, ozone production rates were calculated for the three-week measurement project. The present AQRP project (19-040) focuses on the three analysis tasks described below using the 2017 SAFS data:

Task 1
Quantify the dependence of the ozone production rate on the concentrations of NOx, VOCs, and other measurements at the three SAFS sites where peroxy radical concentrations were measured.

Major findings using these measurements include the following:

1. Ozone formation at the UTSA, Floresville, and Lake Corpus Christi sites was usually under 15 ppb/hr. Multiple lines of evidence show that UTSA was usually NOx-limited except for time periods when primary HOx radical production was low, typically in the morning or because of overcast conditions. Ozone production during these periods was typically less than 5 ppbv/hr.
2. While biomass burning plumes were clearly sampled, there is little evidence from the *in situ* observations that ozone production in these plumes was enhanced when compared to air not influenced by burning emissions.
3. OH reactivity was dominated by biogenic VOCs at both UTSA and Floresville, with isoprene sometimes accounting for over 50% of total OH reactivity. Contributions from alkanes, alkenes, and aromatics were 1% or less at the UTSA site.

Task 2
Conduct zero-dimensional (0-D) photochemical modeling constrained by the SAFS datasets with several model chemical mechanisms for four SAFS measurement sites, spanning a large range of NOx values.

Major findings using these measurements include the following:
1. Two versions of the carbon bond mechanism (CB6r3 and CB05) and the GEOS-Chem mechanism produced peroxy radical concentrations that agreed within 5% of observations. Interestingly, the master chemical mechanism (MCM 3.3.1), which is the most up-to-date and explicit mechanism, overestimated observed peroxy radicals by 27%. Each mechanism was able to reproduce the general observed relationship between ozone production and NO.
2. Ozone production rates at the Travelers' World site, as calculated by the box model, were significantly higher than at UTSA, peaking between 40 and 80 ppbv/hr, depending on the

mechanism. Median NO was more than a factor of two higher at TW, as well. CB6r2, CB05, and GEOS-Chem each suggest possible ozone production in the VOC-limited regime on the order of 20 – 30 ppbv/hr.

3. The dominant peroxy radicals for ozone production at both UTSA and Travelers' World, according to MCM 3.3.1, CB6r3, and GEOS-Chem are HO_2 and radicals derived from isoprene, although isoprene plays a more dominant role at UTSA. Peroxy radicals from alkanes comprised a larger fraction of ozone production at Travelers' World, but still less than half that of isoprene.

Task 3
Apportion ozone concentrations to location-specific emission sources using 3-D air quality modeling with the instrumented Community Multiscale Air Quality model (CMAQ).

Major findings resulting from this modeling work are the following:
1. Consistent with previous studies, the "base" NO_X emissions used as inputs for CMAQ were found to be too high, overestimating concentrations at surface monitors by approximately 50%. Reducing these emissions by 30% brought modeled NO_X to within about 10% of observations.
2. Reducing NO_X emissions by a further 20% lead to median reductions in surface ozone in San Antonio of 2 ppbv over May 2017. Emissions from power plants outside of San Antonio only produced a median of 0.25 ppbv ozone at the surface, although there was significant daily variation, with contributions up to 3 ppbv. NOx emissions from oil and gas operations seem to have minimal impact on San Antonio ozone.
3. The relationship between surface ozone production and NO for high primary HO_X production was similar between CMAQ and observations, with maximum values of about 15 ppbv. Vertical profiles of ozone production show that the highest ozone production rates are limited to near the surface.

Table of Contents

Table of Figures

1. Introduction

The EPA has designated San Antonio and Bexar County as being in marginal non-attainment with the national ambient air quality standard (NAAQS) of 70 ppbv (8-hour average). As a result, regulators will need to make science-based decisions on effective mitigation strategies, including emission reduction programs. Such decisions will require knowledge of the amount of ozone that is transported into the city from upwind (usually Southeast of San Antonio), the absolute rates of ozone formation in and around San Antonio, the relative importance and interaction of various emission sources (e.g., upwind oil and gas activity and urban emissions from the city itself), and when and where ozone formation is NOx-limited or VOC-limited. In contrast to Houston and Dallas, little is known about ozone formation in San Antonio.

During SAFs, measurements were made at the following four sites (primary research team indicated in parentheses):

1. University of Texas at San Antonio, 14 miles northwest of downtown San Antonio (Aerodyne/Drexel)
2. Floresville, 30 miles southeast of San Antonio (Aerodyne/Drexel)
3. Lake Corpus Christi State Park, 100 miles southeast of San Antonio and 40 miles inland from the Gulf of Mexico (Aerodyne/Drexel)
4. Traveler's World RV resort, in the urban core of San Antonio (Baylor/Rice/U. Houston)

These four measurement sites are marked in Figure 1:
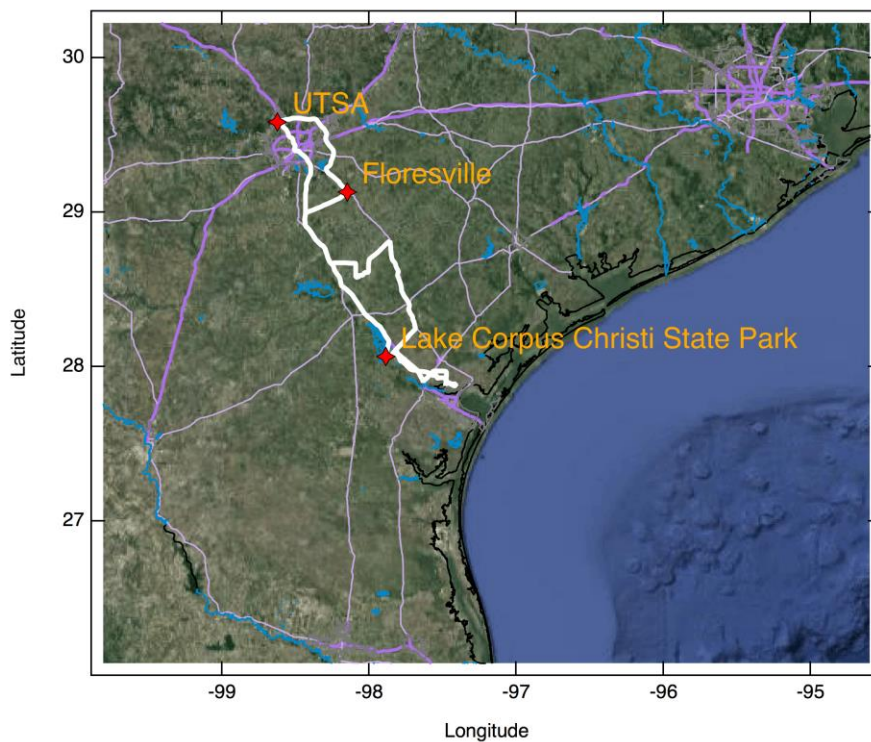
Figure 1. Measurement Locations during SAFS. The red diamond symbols indicate the locations where the mobile labs were stationed. The Traveler's World site is not marked but is in central San Antonio.

Ozone is formed by photochemical reactions involving volatile organic compound (VOCs) and nitrogen oxides (NOx). The photo-oxidation of propane (a component of natural gas) serves as a simple example of this chemistry:

$C_3H_8 + OH + O_2 \rightarrow C_3H_7O_2 + H_2O$ R1
$C_3H_7O_2 + NO \rightarrow C_3H_7O + NO_2$ R2
$C_3H_7O + O_2 \rightarrow CH_3COCH_3 + HO_2$ R3
$HO_2 + NO \rightarrow OH + NO_2$ R4
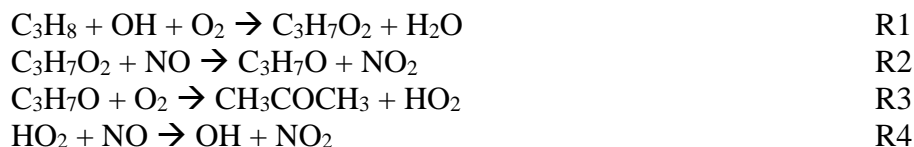
The NO_2 formed by reactions 2 and 4 will undergo photolysis during the day, thereby forming ozone (O_3):

$NO_2 + sunlight \rightarrow NO + O$ R5
$O + O_2 + M \rightarrow O_3 + M$ R6

Thus the rate at which ozone is formed is effectively equal to the rate at which NO is converted to NO_2 by reaction with peroxy radicals (in this case, $C_3H_7O_2$ and HO_2):

$P(O_3) = k_{HO2+NO}[HO_2][NO] + k_{RO2+NO}[RO_2][NO]$ Eq. 1

"RO_2" represents all organic peroxy radicals (e.g., CH_3O_2, $C_2H_5O_2$, etc.)

Due to the various radical termination steps such as formation of H_2O_2 and HNO_3, the value of $P(O_3)$ does not always simply increase with increased concentrations of VOCs or NOx. Ozone production is said to be "NOx-limited" if, due to low NO concentrations, peroxy radicals react with themselves rather than with NO. Conversely, ozone formation is "VOC-limited" (or "NOx-saturated") if HOx radicals (OH, RO_2, HO_2) are mainly lost via reactions with NO_X. Knowing in which chemical regime an air mass resides is crucial for designing effective ozone abatement strategies, since reducing NOx emissions can lead to undesirable *increases* in ozone formation rates if the air is in a VOC-limited state. This is the case in southern California, evident by the higher ozone observed on weekends when there is reduced NOx emissions due to lower diesel truck traffic [*Pollack et al.*, 2012].

The overall objectives of this project are to elucidate the sources of high ozone concentrations in the greater San Antonio area and to conduct analyses that determine if our understanding of ozone formation is accurate. More detailed objectives are to answer the following science questions:

1. What is the dependence of ozone formation in the greater San Antonio area on concentrations of NOx, VOCs, and "HOx" radical precursors? Where is ozone formation "NOx-limited" vs. "VOC-limited"?

2. Do current chemical mechanisms used in 0-D models correctly predict radical concentrations?

3. What are the relative contributions of different emission sources to ozone concentrations in San Antonio?

2. Project Design

To address the above science questions, this project is divided into three tasks described below. Descriptions of the methodologies used and the findings from each task are in sections three, four, and five of this report.

Task 1: Analyze the 2017 SAFS data collected by Drexel and Aerodyne to quantify the dependence of the ozone production rate on supporting measurements.

Task 2: Conduct 0-D photochemical modeling using data from four SAFS measurement sites and compare modeled ozone production rates and peroxy radical concentrations to those calculated using the peroxy radical measurements where available.

Task 3. Apportion ozone concentrations to location-specific emission sources using 3-D air quality modeling with the instrumented Community Multiscale Air Quality model (CMAQ).

3. Task 1

The goal of Task 1 is to analyze the 2017 SAFS data collected by Drexel and Aerodyne to quantify the dependence of the ozone production rate on supporting measurements. A portion of our work on this task consisted of greatly expanding on the preliminary analysis presented in the final report for AQRP project 17-032. These results are described in the following peer-reviewed publication: "Characterization of ozone production in San Antonio, Texas, using measurements of total peroxy radicals", by Daniel C. Anderson, Jessica Pavelec, Conner Daube, Scott C. Herndon, Walter B. Knighton, Brian M. Lerner, J. Robert Roscioli, Tara I. Yacovitch, and Ezra C. Wood, *Atmospheric Chemistry and Physics* 19, 2845–2860, 2019 (accessible at https://doi.org/10.5194/acp-19-2845-2019). Many of the figures below are the same as those that appear in the publication.

3.1 Calculated ozone production rates and dependence on NOx and P(ROx)
Trace gases measured onboard the Aerodyne Mobile Laboratory (AML) and used in this study are summarized here. Unless otherwise indicated, data used in this study were reported as 1-minute averages and then averaged to the 2-minute Ethane CHemical AMPlifier (ECHAMP) time base. Total peroxy radicals (XO_2) were measured with ECHAMP and have an uncertainty of 25%. NO_2 was measured at 1 Hz via Cavity Attenuated Phase Shift (CAPS) spectroscopy [*Kebabian et al.*, 2005; *Kebabian et al.*, 2008]. Nitric oxide (NO) was measured at 0.1 Hz through the same inlet as NO_2 and O_3 using a Thermo Fisher 42i-TL chemiluminescence analyzer, while O_3 was measured with a 2B-Tech model 205 ultraviolet (UV) absorption instrument. Uncertainties (2σ) of the NO, NO_2, and O_3 observations on the ECHAMP measurement time scale are below 5%. The above instruments were zeroed every 15 minutes

with humidity-matched zero air. The zero air was generated by passing ambient air through an Aadco ZA30 Catalyst system for VOC removal and through Purafil Chemisorbant Media, a potassium permanganate based scrubber, for NOx removal.

Quantum Cascade – Tunable Infrared Laser Direct Absorption Spectrometers (QC-TILDAS) from Aerodyne Research Inc. (ARI) were used to measure CO and H_2O (2200 cm^{-1}; measurement wave number), HCHO (1765 cm^{-1}), CH_4 and C_2H_6 (2990 cm^{-1}), H_2O_2 (1277 cm^{-1}), and C_3H_8 (2965 cm^{-1}) [*McManus et al.*, 2015]. A Proton Transfer Reaction – High Resolution – Time of Flight (PTR-HR-ToF) mass spectrometer was used to measure isoprene, acetaldehyde, acetone, benzene, methanol, the sum of monoterpenes, the sum of methyl vinyl ketone (MVK) and methacrolein, and toluene. Typical measurement uncertainties were on the order of 25%. Finally, a prototype of a commercially-available gas chromatograph from ARI with electron-impact time-of-flight mass spectrometer (GC-EI-ToF-MS) was used to measure a suite of VOCs, including isoprene, 1,2,3-trimethylbenzene, ethyl benzene, cyclohexane, *n*-heptane, *n*-hexane, *n*-octane, *n*-pentane, *o*-xylene, and the sum of *m*- and *p*- xylenes. The GC sampled with a multi-component adsorbent trap [*Pollmann et al.*, 2006] for a 5-minute integration period every 20 minutes. GC observations are unavailable for 20-30 May. While toluene and *m*- and *p*- xylene measurement uncertainty was on the order of 20%, typical measurement uncertainties of other observed species, except isoprene, were on the order of 10%.

While there were two independent observations of isoprene, there were limitations with both methods. It was determined that the actual isoprene concentration in the calibration standard used in the field for the PTR had degraded over time, resulting in erroneously high isoprene values. On the other hand, the GC was not calibrated for isoprene during the campaign and observations are only available for half the time. As a result, we use the PTR isoprene from the entire campaign scaled to the GC values, using a GC isoprene sensitivity determined after the campaign. This method results in an estimated isoprene uncertainty of ≈30% (1σ).

Temperature, wind speed, and wind direction were measured at the top of the inlet tower with a 3D RMYoung (Model 81000RE) sonic anemometer. Atmospheric pressure observations used in this study were taken from the National Weather Service observations at the San Antonio International Airport for the UTSA and Floresville sites and from the Corpus Christi International Airport for the Corpus site. NO_2 photolysis frequencies (J_{NO2}) were measured via a filter radiometer (MetCon, GmbH) located on top of the AML [*Shetter et al.*, 2003; *Stark et al.*, 2007].

3.2 Calculated ozone production rates and dependence on NOx and P(ROx)
The gross ozone production rate $P(O_3)$ was calculated by the following equation:

$$P(O_3) = 8.5 \times 10^{-12} ([RO_2]+[HO_2])][NO]. \quad \text{Eq. 2}$$

More accurately, this is described as the gross rate of Ox formation, where [Ox] is equal to the sum of [NO_2], [O_3], and [O]. The sum of [RO_2] and [HO_2] was measured by Drexel's ECHAMP instrument during SAFS at the UTSA, Floresville, and Lake Corpus Christi sites (but not the Traveler's World site). 8.5×10^{-12} is the rate constant for the reaction $HO_2 + NO \rightarrow OH + NO_2$, which is within 10% of the k values for the reaction of NO with CH_3O_2 and isoprene RO_2 [*Orlando and Tyndall*, 2012]. The 2σ uncertainty in this calculated gross ozone production rate is

34%, calculated by adding the uncertainties for the rate constant, peroxy radical concentrations, and NO concentrations in quadrature.

The net ozone production rate can be calculated by subtracting from the above term the chemical losses of O_X, i.e. the reaction of $O(^1D)$ with H_2O; the reaction of O_3 with OH, HO_2 and alkenes; and the reaction of NO_2 with OH.

We define "ROx" as the sum of OH, HO_2, and organic peroxy radicals RO_2: $[ROx] = [OH] + [HO_2] + [RO_2]$. The rate at which ROx radicals are formed has a key role in determining O_3 formation rates. We calculate the ROx production rate P(ROx) using the following equation:

$$P(ROx) = 2j_{(O1D)}[O_3](k_{O1D+H2O}[H_2O]/(k_{O1D+H2O}[H_2O] + k_{O1D+O2}[O_2] + k_{O1D+N2}[N_2]))$$
$$+ 2j_{HCHO \to H + CHO}[HCHO] + 2j_{CH3CHO \to CH3 + HCO}[CH_3CHO] + 2j_{H2O2}[H_2O_2] +$$
$$2j_{Acetone}[CH_3COCH_3] + j_{HONO}[HONO] \quad \text{Eq. 3}$$

HONO was not measured during SAFS but was estimated based on the observed HONO/NOx ratios observed in Houston in 2009 (0.04 at most). Similarly, the contribution of alkene ozonolysis to P(ROx) was evaluated using measured and estimated alkene concentrations and was found to be negligible. At all sites, P(ROx) was dominated by the first two terms above (photolysis of O_3 followed by reaction of $O(^1D)$ with H_2O, and HCHO photolysis).

All of the measured concentrations of ozone, total peroxy radical concentrations ("XO_2" = $[RO_2]$ + $[HO_2]$), NO, NO_2 photolysis rate, and calculated ozone production rates are shown in Figure 2.
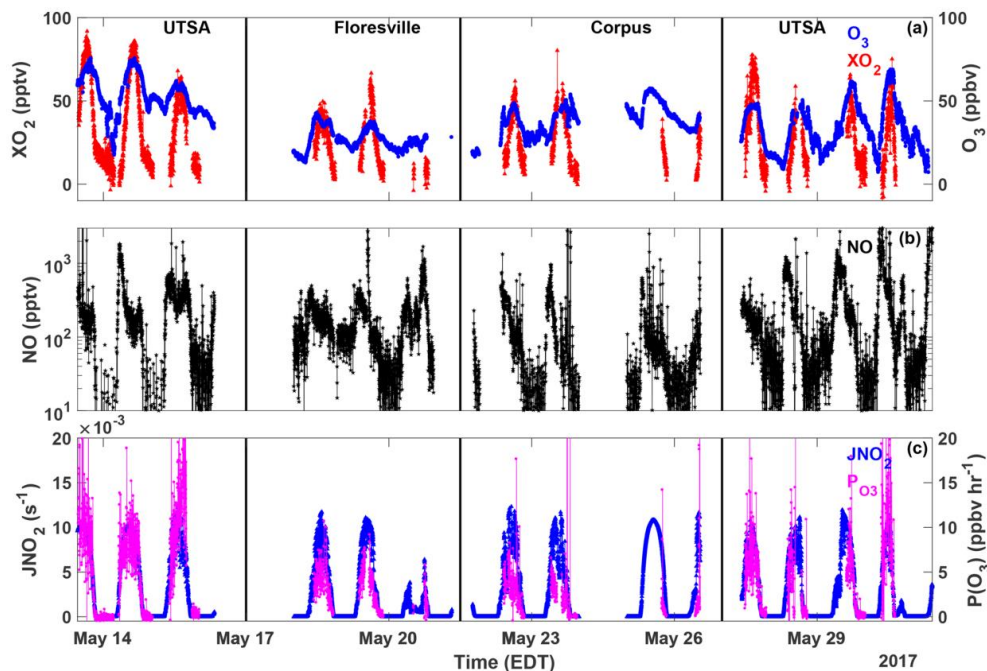
Figure 2. Time series of [NO], $[RO2]+[HO_2]$, $[O_3]$, jNO_2, and $P(O_3)$ from SAFS. Time shown is Eastern Daylight Time (= Local time + 1 hours). All measurements are 15-minute averages.

Distributions of these values, including isoprene, are shown in Figure 3 below:
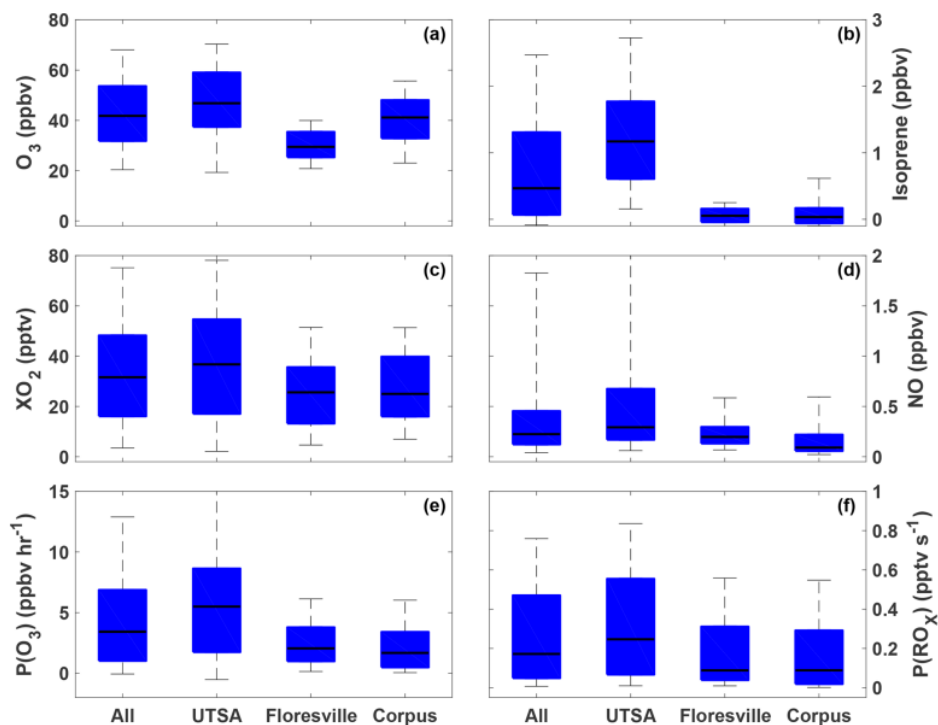
Figure 3. Distributions of [NO], [RO$_2$]+[HO$_2$], [O$_3$], isoprene, P(O$_3$), and P(ROx) from SAFS. Median values are indicated by the black lines, and the 5th, 25th, 75th, and 95th percentiles are shown by the edges of the boxes and whiskers.

A large part of Task 1 was characterizing the dependence of P(O$_3$) on NOx, VOC reactivity, P(ROx), and other measures. At fixed VOC reactivity and P(ROx) value, the ozone production rate is expected to increase with increasing NOx concentrations until a certain threshold value. At high NOx concentrations ozone production rates decrease with further increases in NOx because the reaction OH + NO$_2$ + M → HNO$_3$ + M can reduce OH concentrations. When P(O$_3$) increases with NOx, ozone formation is referred to as "NOx-limited", whereas when P(O$_3$) decreases with NOx, ozone formation is referred to as "VOC-limited" or "NOx-saturated". At the three SAFS sites where we measured peroxy radicals, ozone formation appeared to be NOx-limited based on the inspection of the graphs of P(O$_3$) vs. NO (Figure 4). Increasing P(ROx) is expected to always increase P(O$_3$). Under NOx-limited conditions, the ozone production rate is expected to be almost independent of the VOC reactivity. The dependence of P(O$_3$) on NO, P(ROx), and VOC reactivity is shown in Figure 4.
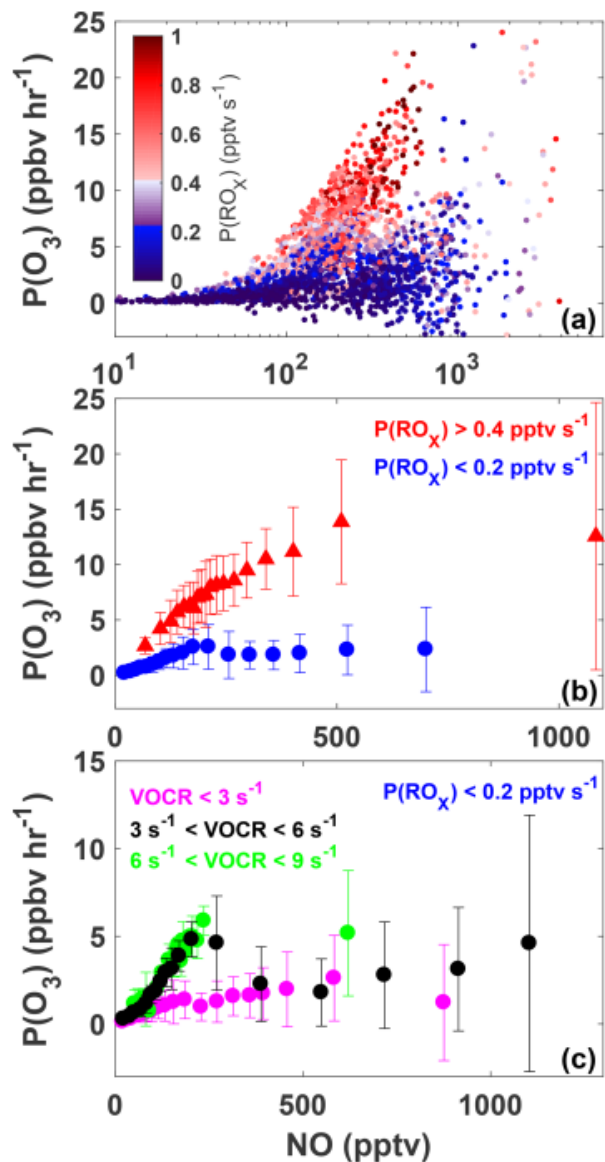
Figure 4. Dependence of P(O₃) on NO, P(ROx), and VOC reactivity for all daytime observations (07:00 to 20:00) from UTSA, Floresville, and Corpus.

Increased P(ROx) values do indeed lead to increases in P(O₃). Panel b of Figure 4 bins the data into a range of NO values and either "low" P(ROx) values (less than 0.2 ppt/s) or "high" P(ROx) values (greater than 0.4 ppt/s). Under high P(ROx) values, P(O₃) increases with NOx until at least 500 ppt NO, suggesting P(O₃) was NOx-limited for [NO]<500 ppt. There are few points at high P(ROx) and with [NO]> 500 ppt. Under low P(ROx) conditions (mostly overcast conditions), P(O₃) appears to reach the turnover [NO] value of about 200 ppt. This indicates that while ozone formation is VOC-limited during those times, those time periods, which account for only 20% of the SAFS observations, are also characterized by low ozone formation rates – less than 5 ppb/hr. For the high P(ROx) conditions, ozone formation rates can be above 10 ppb/hr.

The dependence of P(O$_3$) on the VOC reactivity (Figure 4, panel c) under low P(ROx) was an interesting result. When the VOC reactivity was "medium" (between 3 and 6 s^{-1}) or high (between 6 and 9 s^{-1}), there was little effect on P(O$_3$), as expected from the traditional understanding of ozone chemistry [*Kleinman*, 2005]. At the lowest VOC reactivity values, however (less than 3 s^{-1}), very low P(O$_3$) values were observed.

3.3 Dependence of P(O$_3$) on biomass burning markers
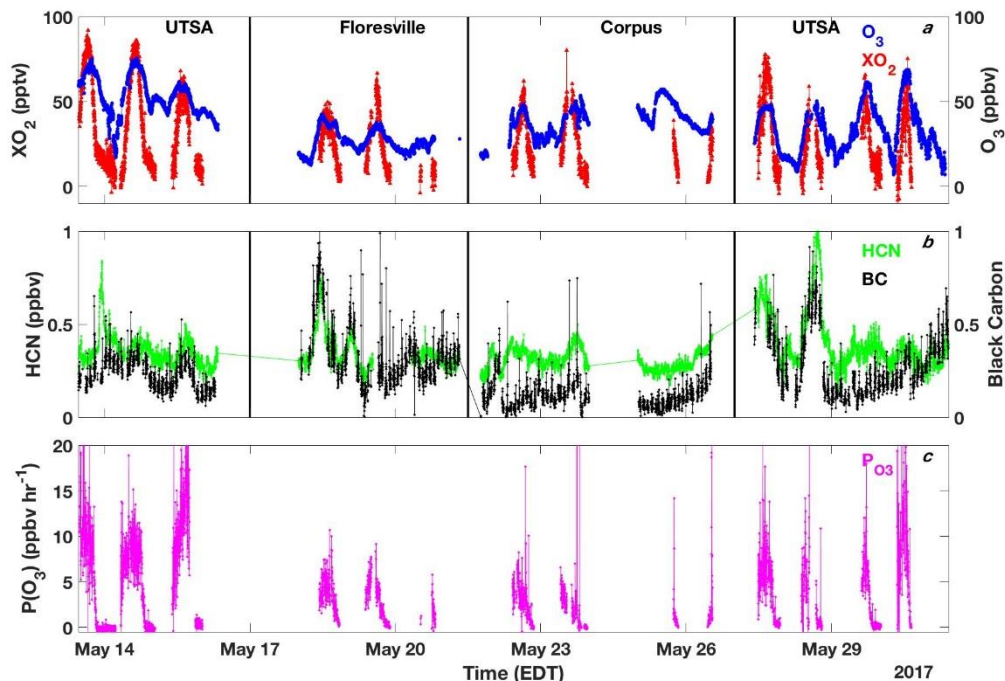
Figure 5. Time series of concentrations of peroxy radicals (XO$_2$), O$_3$, HCN, black carbon, and ozone production rates. A range of HCN values were observed, suggesting a variable influence from biomass burning.

The influence of biomass burning on ozone concentrations and ozone formation rates is not well understood [*Jaffe and Wigder*, 2012]. Though fires emit VOCs and NOx – the ingredients needed for ozone formation, the large amounts of primary particulate matter emitted and possibly the secondary particulate matter that forms in the atmosphere can reduce photolysis rates, which would have a negative effect on ozone formation by reducing the rate of ROx formation (e.g., reduced photolysis of formaldehyde). Furthermore, heterogeneous reactions of the smoke with ozone itself and ROx radicals can reduce O$_3$ concentrations.

Figure 5 shows the time series of *in situ* observations of O$_3$, XO$_2$, P(O$_3$), and the biomass burning tracers hydrogen cyanide (HCN) and black carbon (BC). The tight correlation and elevated concentrations of HCN and BC suggest that the AML measured biomass burning influenced air on multiple occasions at both the Floresville and UTSA sites. For comparison, subsequent measurements by the Aerodyne mobile laboratory in McCall, Idaho during the summer of 2018 showed a similar range of HCN values (rarely above 1 ppb).

Figure 6 shows the distribution of O$_3$ and P(O$_3$) for biomass burning influenced air as well as air not influenced by biomass burning emissions. We define 75th and 95th as air parcels where both

HCN and BC were both above the 75th and 95th percentile of observations for the duration of the campaign. "No fire" indicates observations where both HCN and BC were below the 75th percentile. At the UTSA site, both O_3 and $P(O_3)$ were depressed in the biomass burning air parcels as compared to the "No fire" case, with median O_3 lower by ~10 ppbv and median $P(O_3)$ lower by 2 ppb/hr for the 75th percentile case. The opposite signal was observed at Floresville, with higher O_3 and $P(O_3)$ for the biomass influenced air parcels.
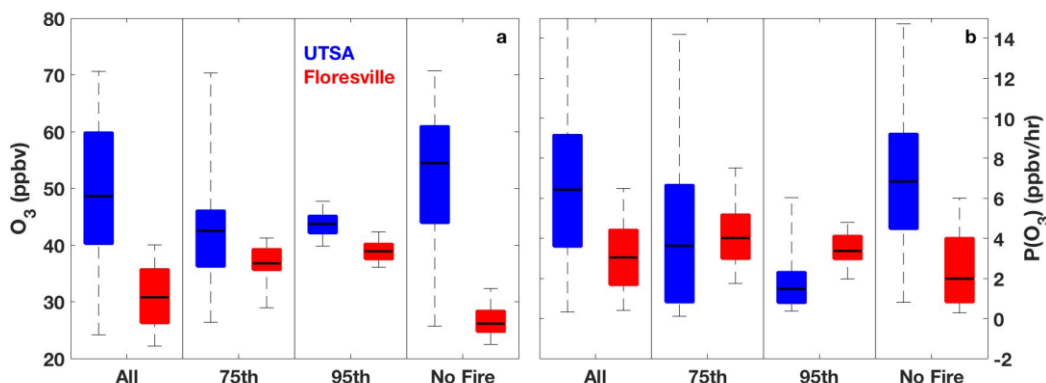
Figure 6. Distribution of [O_3] and $P(O_3)$ between 07:00 and 20:00 at UTSA and Floresville. 75th and 95th are observations where concentrations of HCN and black carbon were above the indicated percentile. "No fire" indicates observations were both HCN and black carbon were below the 75th percentile.
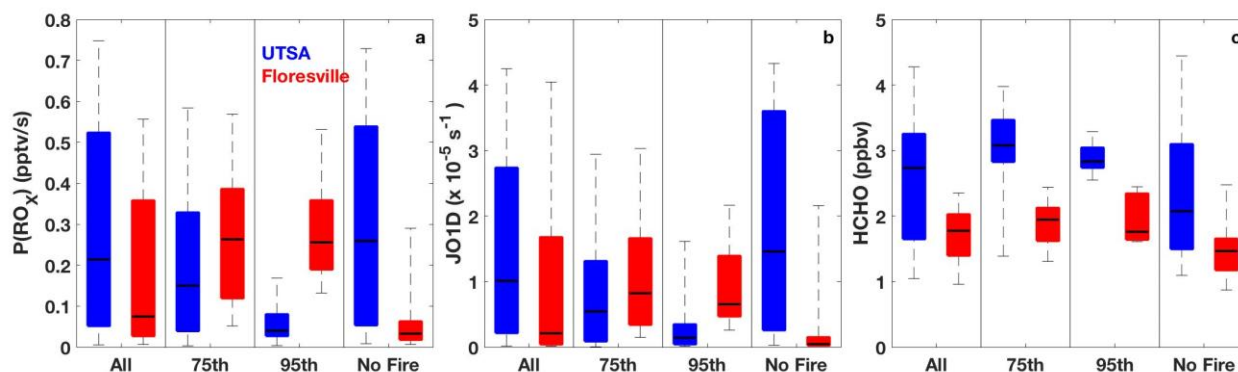
Figure 7. Distribution of $P(ROx)$, [HCHO], and $J(O^1D)$ between 07:00 and 20:00 at UTSA (blue) and Floresville (red).

To determine the source of these differences, we can explore variations in $P(ROx)$, as higher $P(ROx)$ tends to lead to higher O_3 production. Figure 7 shows the distribution of $P(ROx)$, $J(O^1D)$, and HCHO (the two dominant terms in calculating $P(ROx)$, for the UTSA site. Again, $P(ROx)$ is depressed for the biomass burning cases as compared to the "no fire" air parcels. This decrease is being driven, however, by decreases in $J(O^1D)$, which affects the $P(ROx)$ term more strongly than the increase in HCHO. The opposite trend is seen at Floresville. This suggests that the differences in O_3 and $P(O_3)$ at the two sites for the biomass burning influenced air parcels are likely driven by differences in insolation. With the limited number of observations we are limited to it is difficult to draw any conclusions regarding the influence of biomass burning on ozone

concentrations in San Antonio. At UTSA, the days with the greatest biomass burning influence had the lowest ozone concentrations and formation rates, but that might simply have been because those days happened to be the most overcast days. The opposite trend was observed in Floresville.

3.4 Satellite retrieval of HCHO and NO₂ columns

The NOx-limited nature of ozone formation is also supported by the ratio of the HCHO column to the NO$_2$ column using satellite retrievals. We use observations of HCHO and NO$_2$ from the Ozone Monitoring Instrument (OMI), which provides daily coverage based on differential optical absorption spectroscopic retrievals using backscattered UV-visible solar radiation. For ratios of greater than 2 are generally considered to indicate NOx-limited ozone formation (Duncan et al. 2010, Ring et al; 2018), although the spatial averaging does not preclude the existence of smaller geographic regions in which ozone formation could be VOC-limited.
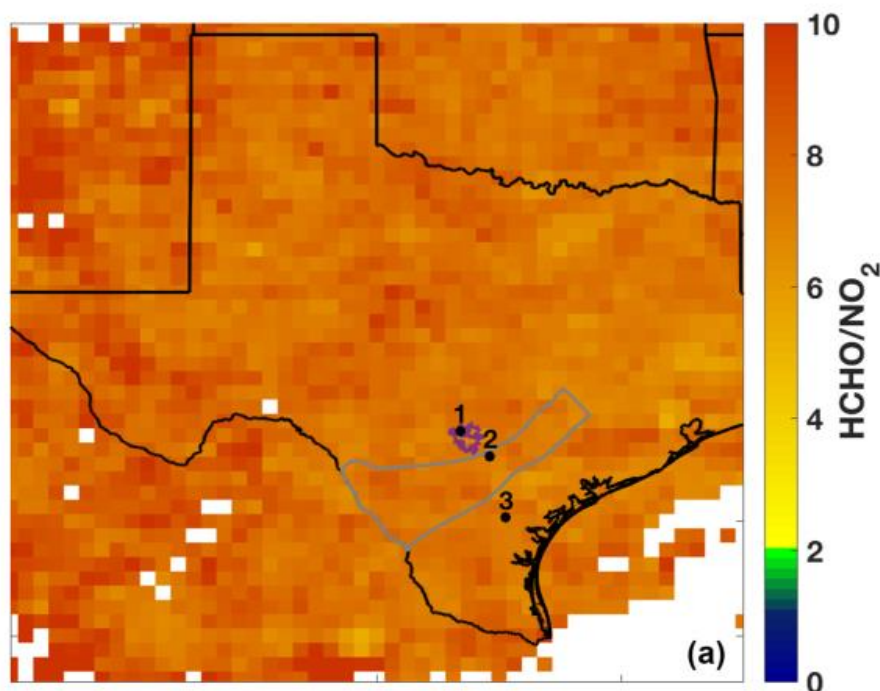
Figure 8. The ratio of total column HCHO to tropospheric column NO$_2$ averaged over the months of May through July 2017. The outlines of the Eagle Ford Shale (grey) play and San Antonio city limits (purple) are also shown for reference

3.5 OH reactivity

The overall OH reactivity was calculated using the following equation:

OH reactivity = $\sum k_{OH+X}[X]$ Eq. 4

where X represents each compound that can react with OH and k_{OH+X} is the rate constant for the reaction of X with OH. At UTSA, biogenic VOCs, in particular isoprene, accounted for over half of the total OH reactivity in the afternoon (Figure 6). Alkanes accounted for at most 5% of the OH reactivity during SAFS. In Floresville, which is upwind of the city during prevailing

Southeasterly flow, the OH reactivity is from several classes of compounds, including CO, carbonyls (mostly formaldehyde), biogenic VOCs, and methane. The relative contribution to OH reactivity of various VOCs is very similar to their contribution to ozone formation. Given that ozone formation is usually NOx-limited, at least at UTSA, Floresville, and Lake Corpus Christi, reducing VOC emissions would not be expected to significantly affect ozone formation rates.
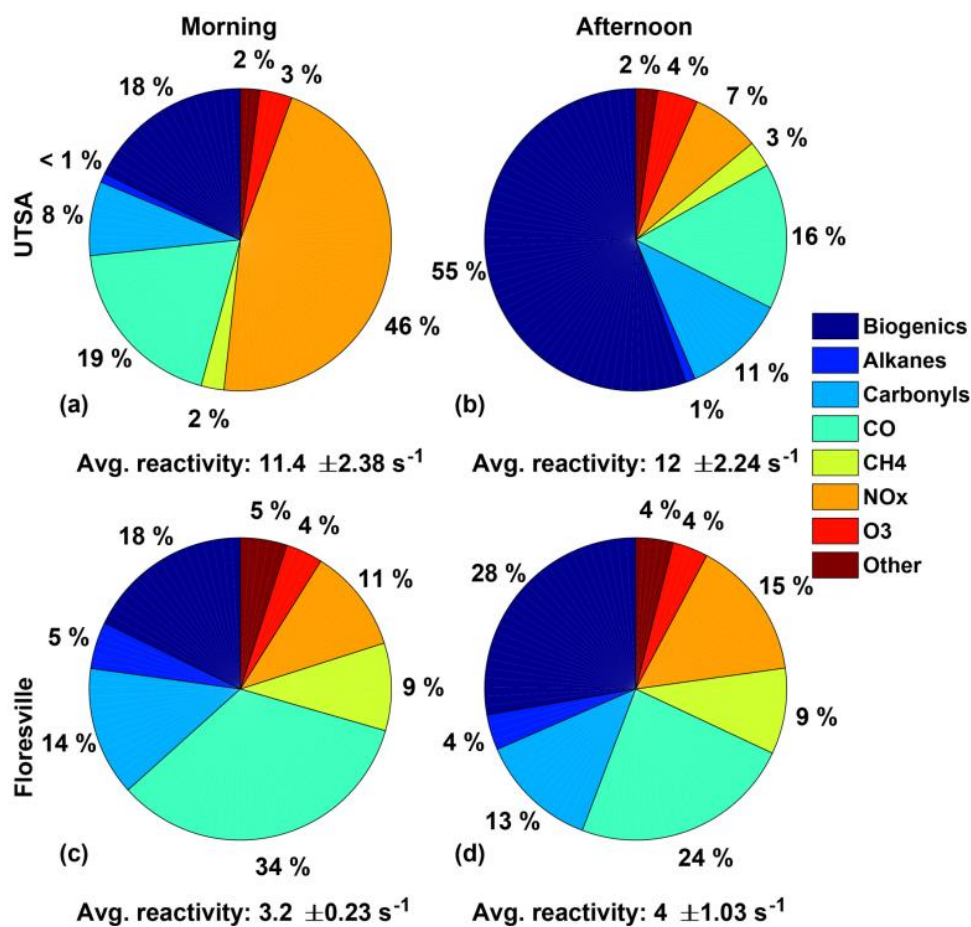
Figure 9. OH reactivity in the morning (07:00 – 11:00) and afternoon (13:00 and 20:00) at UTSA and Floresville.

4. Task 2

4.1 Observations at Travelers' World

In order to model XO_2 and $P(O_3)$ in downtown San Antonio, we also use observations made by Baylor University and the University of Houston (BU/UH) at the Travelers' World site from 12 to 25 May. In addition, these groups were at UTSA from 27 to 30 May along with the AML, providing the opportunity to compare observations and modeling results between the two observation sets. The species used in this study and the observation method are shown in Table 1. The data used here have been averaged to a 5-minute time base.

Table 1. Species observed by BU/UH used in the box modeling analysis

Species	Instrument/Technique
NO	Thermo 42-i TL chemiluminescence
NO_2	AQD with photolytic converter
CO	Cavity Ring Down Spectroscopy (Los Gatos)
Isoprene, HCHO, CH_3CHO, Acetone, Benzene, Monoterpenes, Toluene	PTR-MS Ionicon
CH_4, C_2H_6	QC-TILDAS
O_3	UV Absorption (2B Tech)
Ethene, Propene, cis-2-Butene, trans-2-Butene, 1-Pentene	Whole Air Sampling

In general, observations made by BU/UH at UTSA agreed with those made by the AML within 10% and had high correlation ($r^2 > 0.8$). Species with the largest differences include NO (AML 18% higher, $r^2 = 0.91$), C_2H_6 (AML 17% higher, $r^2 = 0.99$), and HCHO (AML 0.23 ppbv higher, $r^2 = 0.55$).

AML observations used in this study are described in section 3.1.

4.2 Box Model

Ozone production and XO_2 at the three AML sites and at Travelers' World were modeled with the Framework for 0-D Atmospheric Modeling (F0AM) version 3.1 box model [*Wolfe et al.*, 2016b]. The model was run with four different chemical mechanisms: a subset of the Master Chemical Mechanism [*Jenkin et al.*, 2003; *Saunders et al.*, 2003] version 3.3.1 (MCMv331) [*Jenkin et al.*, 2015], two versions of the carbon bond mechanism, CB05 and CB6r3, and the chemical mechanism of GEOSChem, version 11-02d. MCMv331 is a near-explicit mechanism that allows for the evaluation of the state of the science of XO_2 and $P(O_3)$ chemistry. In contrast, the other three mechanisms are lumped and used primarily in 3 dimensional air quality models (*e.g.* CMAQ and CAMx for CB05 and CB6r2). Use of these mechanisms provides a computationally inexpensive method to evaluate the chemistry within air quality models. For a more thorough comparison of the different mechanisms, see *Marvin et al.* [2017].

The model was run for air parcels observed at the UTSA and Floresville AML sites. Results from Corpus are excluded from this analysis because the GCMS was inoperable at that time.

F0AM was constrained with observations of temperature, pressure, water vapor, O_3, NO_2, CO, CH_4, HCHO, methanol, acetone, acetaldehyde, isoprene, propane, ethane, ethyne, monoterpenes, toluene, *n*-pentane, *n*-hexane, *n*-heptane, *n*-octane, xylenes, ethyl benzene, 1,2,4-trimethylbenzene, benzene, and cyclohexane. Because there were no speciated observations, all monoterpenes were assumed to be α-pinene. Likewise, observations of total *m*- and *p*-xylene were assumed to be a 50% mixture. The AML did not make observations of anthropogenic alkenes during SAFS. Concentrations were estimated from an GC at the nearby EPA Camp Bullis site and included in a separate model run. There was no apparent change in modeled XO_2 or $P(O_3)$ when these alkenes were included, so we omit them from this analysis.

In addition, the box model was run for the BU/UH observations at both the TW and UTSA sites. The model was constrained to the same species as the AML, with the exception of the xylenes, ethyl benzene, 1,2,4-trimethylbenzene, and methanol, which were unavailable. Longer chain alkanes (cyclohexane, *n*-pentane, *n*-hexane, *n*-heptane, and *n*-octane) were made at infrequent intervals using whole air sampling. To estimate the concentrations of these species for the modeled data points, concentrations were regressed against benzene for the whole air samples, and the resulting relationship was used to estimate their concentration from the higher frequency benzene observations made by the PTRMS. In addition, it was found that anthropogenic alkenes could impact the results at the TW site. Concentrations of ethene, propene, cis- and trans- 2-butene, and 1-pentene, all measured with whole air sampling, were estimated using the same method as for long chain alkanes.

Observational constraints were averaged over the 2-minute ECHAMP sampling interval for the AML and a 5-minute time base for the BU/UH observations. Only intervals with simultaneous observations of CO, O_3, NO, water vapor, isoprene, and HCHO were used. In addition, for the AML sample intervals, XO_2 observations were also required. Missing data for other species were linearly interpolated in time if there were observations within two hours before and after a given sampling interval. Otherwise missing data were estimated from site specific diurnal profiles produced from observations at each site. Data from the GC, which had a sampling frequency slower than that of ECHAMP, were linearly interpolated to the ECHAMP sampling time. The modeled intervals were further restricted to sampling at a solar zenith angle (SZA) less than 80°.

For photolysis reactions, the model was constrained to observations of J_{NO2}. Other photolysis rates were determined from a lookup table of values calculated by the TUV model as described in *Wolfe et al.* [2016b]. These values were then scaled to the observed JNO_2. The model was run forward in time with a model time-step of 1 hour, with all constrained concentrations and meteorology held constant but photolysis frequencies varying with time of day. The diurnal cycle was repeated for 4 days for each set of observations, which was found sufficient to bring XO_2 into steady state.

Major sources of uncertainty in the box model include the measurement uncertainties in the observations used to constrain the model as well as the choice of method for NO_X constraints. To estimate total uncertainty of modeled XO_2 and $P(O_3)$, we use the method described in *Anderson et al.* [2017]. First, we perturb one of the model constraints by the observational uncertainty, leaving all other model inputs undisturbed. We then calculate the change in

modeled $P(O_3)$ and XO_2 from the baseline run. We then repeat this process for all constrained model species as well as for JNO_2. In addition, we also reran the model constrained to NO and to total NO_X. We then added the percent change in model values in quadrature. This resulted in a total uncertainty of 17% and 44% for XO_2 and $P(O_3)$, respectively, with the major sources of uncertainty for both values being JNO_2 and the method for constraining NO_X. Model uncertainties are in line with the uncertainties in the observed species (25% and 34% for XO_2 and $P(O_3)$, respectively). This method does not, however, take into account uncertainties associated with rate constants so is a lower limit.

4.3 Results

4.3.1 Comparison between observations at UTSA and TW

While median O_3 at UTSA and TW were similar, the distributions of NO and isoprene, both important species for O_3 production, were different, suggesting possible differences in the O_3 production regime in the two areas of San Antonio. Median O_3 was 12% higher at UTSA than at TW, although the overall distributions are almost identical. Median O_3 at Floresville, the AML site immediately upwind of San Antonio, had significantly lower O_3 than both city sites, with the 95th percentile of observations at Floresville lower than the median values in San Antonio.
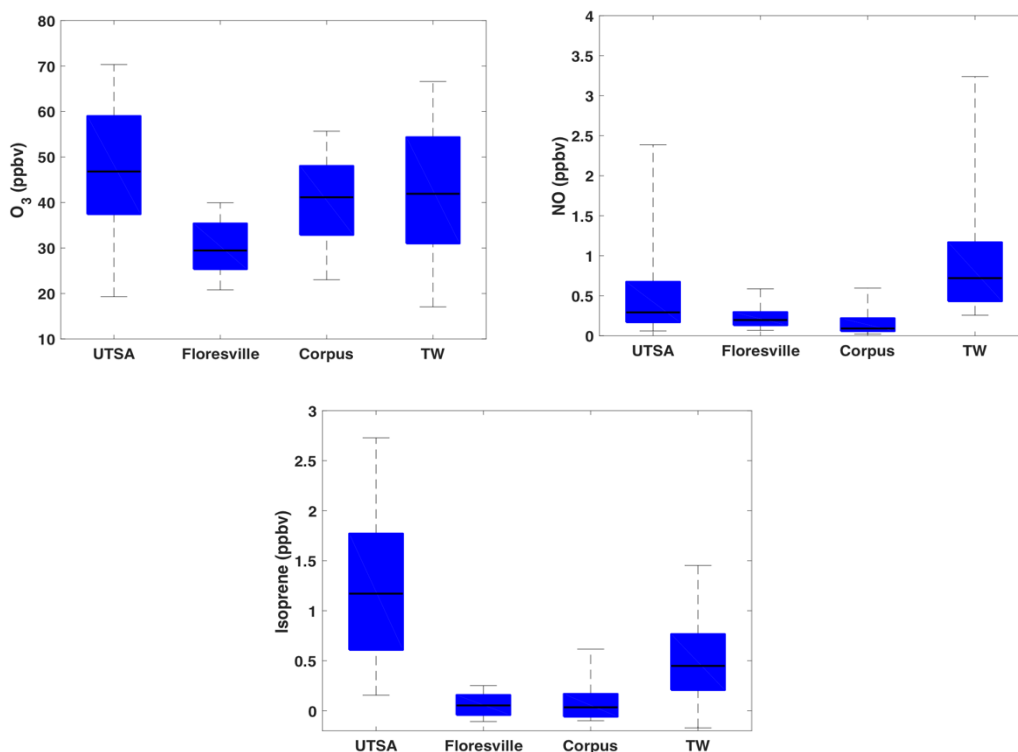
Figure 10. Distribution of O_3 (**a**), NO (**b**), and isoprene at the four different SAFS sites. Data are for daytime (07:00 – 20:00 EDT) only. XO_2 and $P(O_3)$ for the TW site are from the F0AM model. The 5th, 25th, 50th, 75th, and 95th percentiles are shown by the edges of the whiskers, box, and black line.

In contrast, median NO was 2.5 times higher at TW than at UTSA, with almost half of the TW observations above the UTSA 75th percentile. This difference in concentrations is likely due to the significantly higher mobile emissions in the downtown region, as compared to the comparatively remote UTSA site. Isoprene, on the other hand, was more than a factor of 2 higher at UTSA than at TW, a result of a larger forested area near UTSA and the short lifetime of isoprene.

We have shown, using the *in situ* observations, that ozone formation at the UTSA site is almost exclusively NO$_X$ limited, with the exception of early morning, when P(O$_3$) is normally below 5 ppbv/hr. The large difference in NO and isoprene concentrations between UTSA and TW suggests that ozone production in downtown San Antonio could differ from the outskirts of the city. Because UH/BU did not make XO$_2$ observations or direct measurements of P(O$_3$), we must use a box model to calculate these values at the TW site. First, we model these values at UTSA and Floresville, to determine the model's skill at reproducing observations from the AML, and we then use the BU/UH observations to model ozone production at TW.

4.3.2 Box Model Results at UTSA
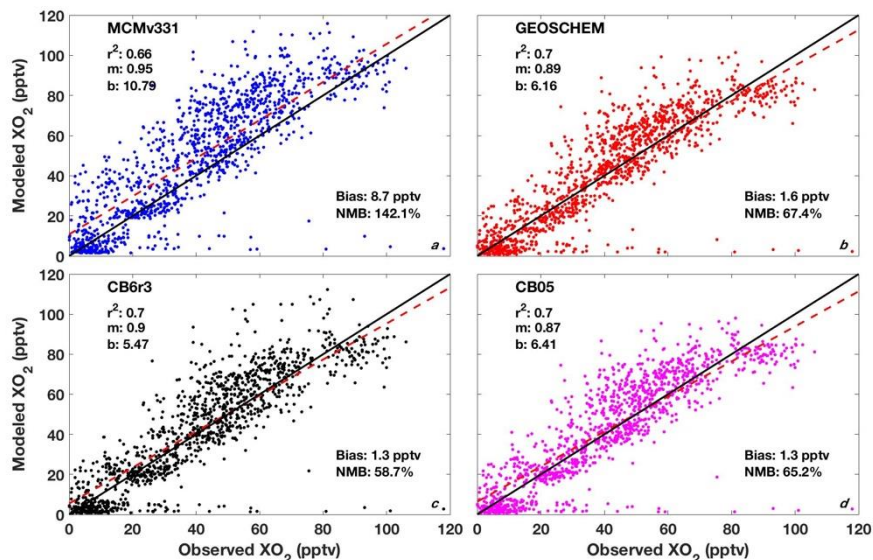
Figure 11. Linear least squares regression of observed XO$_2$ at UTSA and Floresville against modeled values using the MCMv331 (**a**), GEOSChem (**b**), CB6r3 (**c**), and CB05 (**d**) chemical mechanisms. The slope (m), intercept (b), and r^2 value, as well as the mean bias and normalized mean bias (NMB) for each regression is also shown.

Each chemical mechanism investigated here (MCMv331, GEOSChem, CB605, and CB6r3) was able to reproduce the observed XO$_2$ at the Floresville and UTSA sites within 30% for observed concentrations above 20 pptv. A regression between observations and box model output is shown in Figure 11. The regression for each mechanism has high linearity (r^2 > 0.65), and model bias ranges from 8.7 pptv for MCMv331 to -0.4 pptv for GEOSChem. Normalized mean bias (NMB) was significantly higher, ranging from 142% for MCMv331 to 58.7% for CB6r3. This bias is driven by differences at low concentrations. When NMB is calculated for observed concentrations above 20 pptv, this range decreases to 5% to 23%. We note that the excellent

agreement is likely fortuitous given the uncertainties associated with the observations and model. See section 4.2 for a discussion of model uncertainty.

Although the bias was highest for MCMv331, there is little difference in total modeled XO_2 for the different mechanisms. Each mechanism tends to underestimate the observed XO_2 at the highest concentrations. For observed XO_2 values between 80 and 100 pptv, each mechanism plateaus, with near constant XO_2 over the entire range. It is possible that, at these concentrations, the mechanisms are removing XO_2 from the system, either through self-reactions or reaction with NO, at rates higher than in reality. Given the large differences in the complexity of isoprene chemistry, the similar performance of CB05 and CB6r3 is somewhat surprising. *Marvin et al.* [2017] show that CB6r2, a mechanism that varies slightly from the one used here, could reproduce observed HCHO with much higher fidelity than CB05. This suggests that the accuracy of the results presented here likely depends on the quality of the HCHO measurements and that, for 3 dimensional model, CB05 performance would likely be less accurate given the relative simplicity of its isoprene chemistry. Both the model behavior at higher XO_2 and the dependence on HCHO observations warrant further investigation. We have not been able to definitively explain the existence of the locus of points for which the modeled concentrations are low (< 20 ppt) but the measured values range up to 100 ppt in Figure 11. We suspect it is due to an error in how the model was run. It is very unlikely that the model would truly predict such low concentrations when there is always some amount of photolysis of ozone and formaldehyde. This would hold true even if there was appreciable contribution of radical formation from "non-traditional" radical precursors like $ClNO_2$ and Cl_2.
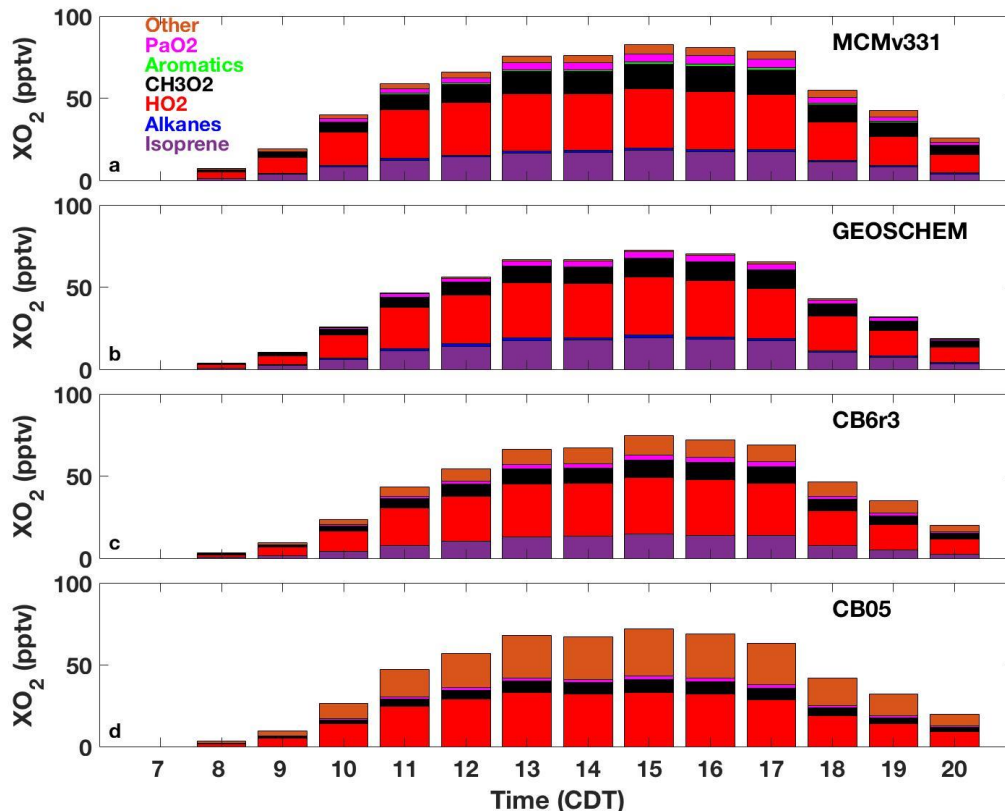
Figure 12. Mean diurnal profile of different XO_2 species at UTSA for MCMv331 (**a**), GEOSChem (**b**), CB6r2 (**c**), and CB05 (**d**). See text for a description of the different categories.

While total XO_2 is similar among the different models, the concentrations of individual XO_2 constituents differ somewhat. The average diurnal profile of XO_2 from the different mechanisms is shown in Figure 12. For each mechanism, we show the mean concentrations of HO_2, CH_3O_2, and the peroxy acetyl radical (PaO_2). In addition, we have grouped the other XO_2 species into the categories Isoprene, Alkanes, and Aromatics. Each of these categories contains first generation and additional peroxy radicals that derive exclusively from species in that category. For example, the isoprene category contains not only isoprene RO_2 species, but also, among others, peroxy radicals derived from methyl vinyl ketone and methacrolein. The Other category contains species that do not fit into any of the other category or species that can be derived from multiple sources. Because of the lumping used in the carbon bond mechanism, it is not possible to distinguish alkane derived XO_2 from some other sources, so these species are included in the Other category. For the same reason, isoprene derived XO_2 for CB05 is also included with Other.

In general, each mechanism agrees that the largest contributor to total XO_2 is HO_2, with significant contributions from the Isoprene group and CH_3O_2. Alkanes and aromatics, on the other hand, generally comprised less than 2% and 1% of the total, respectively. Excluding the other category, GEOSChem and the MCM performed similarly. For example, for 13:00 EDT, concentrations of isoprene RO_2 and HO_2 agreed within 5% between the two models, well within model uncertainty. This suggests that differences between MCMv331 and the other mechanisms likely stem from the increased number of reactions and additional species. CB6r3 performed

similar to GEOSChem and MCMv331 for HO_2, although the isoprene RO_2 contribution was about 25% lower than for the other two mechanisms. Total XO_2 from CB05 is comparable to GEOSChem and CB6r3. It is likely that the influence from isoprene is larger than suggested by this analysis. Because isoprene is one of the main sources of HCHO in forested areas [*Wolfe et al.*, 2016a] and HCHO is one of the predominant HO_2 sources [e.g. *Volkamer et al.*, 2010], some fraction of the HO_2 is also derived from isoprene oxidation.
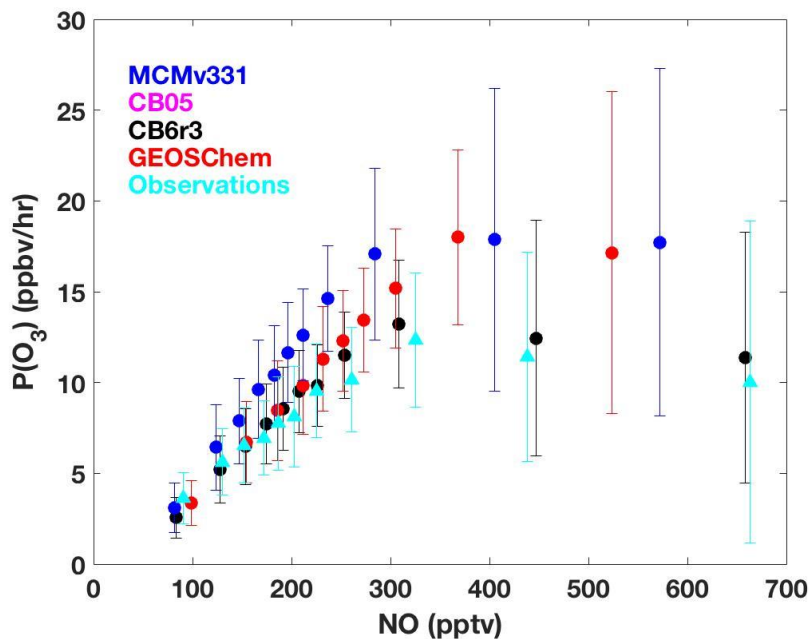
Figure 13. Relationship between $P(O_3)$ and NO for the four chemical mechanisms and observations at the UTSA site. Only showing results for points where $P(RO_X) > 0.4$ pptv/s. Data are mean values for NO bins with an equal number of observations in each bin. Error bars represent one standard deviation.

Consistent with the XO_2 results, each chemical mechanism captures the overall relationship between $P(O_3)$ and NO. Figure 13 shows this relationship for $P(RO_X)$ rates greater than 0.4 pptv/s. While each mechanism does show an increase in $P(O_3)$ with NO until about 300 pptv and then a slight decrease or plateau above this value, they do differ slightly in magnitude, with the MCMv331 consistently overestimating $P(O_3)$ and CB05 consistently underestimating the value. CB6r3 agrees well with observations for all NO values, while GEOSChem overestimates $P(O_3)$ above 300 pptv. While there is some disagreement, values agree within the combined measurement and model uncertainty.

One source of this disagreement between observation and model is the way the box model constrains NO_X. Due to its design, F0AM can either be constrained to NO, NO_2, or total NO_X. Here, we have constrained the model to observed NO_2 because this method results in modeled NO values that are generally within 30% of observed values. Both of the other two methods of constraining the model results in larger disagreement with observed NO_X species. As described in the model uncertainty section, the NO_X constraint is the largest overall contributor to uncertainty of modeled NO_X, accounting for about half of the total 44% uncertainty. The

modeling method we have used results in the discrepancy in the size of the NO bins in Figure 13 for each mechanism and likely contributes to disagreement in the mean P(O₃) values.
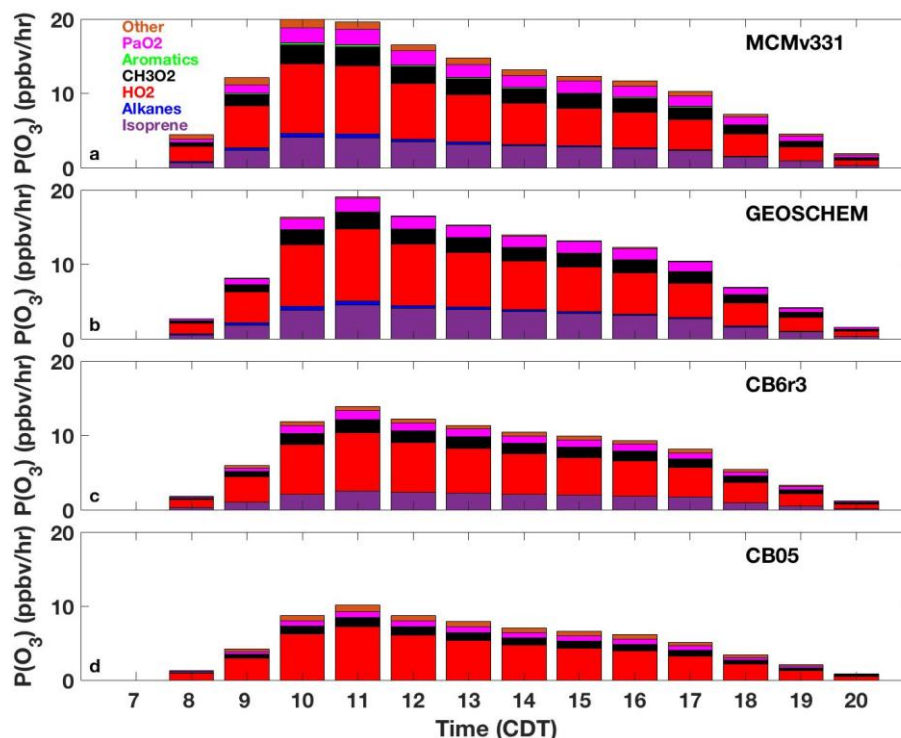
Figure 14. Same as Figure 12 except for P(O₃).

The dominant contributors to P(O₃) from all four mechanisms are HO₂ and isoprene RO₂, consistent with the speciation of total XO₂ and the observed OH reactivity. Figure 14 shows the diurnal profile of P(O₃) as calculated with each mechanism and broken down by XO₂ type, as described earlier. Each mechanism suggests a peak in P(O₃) at 10:00 or 11:00 CDT. During this time, isoprene RO₂ contribution to P(O₃) ranges from 18% for CB6r3 to 26% for GEOSChem. The HO₂ contribution ranges from 47% with the MCM to 71% for CB05, with both GEOSChem and CB6r3 attributing 56% of P(O₃) to HO₂.

We have shown that F0AM and each chemical mechanism studied here is able to reproduce observed XO₂ and P(O₃) within combined measured and modeled uncertainty at the UTSA site. Using the information found in this analysis, we can then model these quantities at TW using the BU/UH dataset.

4.3.3. Box Model Results at TW
Before modeling data at TW, we first compare modeled P(O₃) using the AML data and the BU/UH data at the UTSA site on May 30, 2017. While there was overlap in obsrvations at the UTSA site from May 28 to May 30ᵗʰ, there were frequent times during the first two days when

instruments vital to box modeling were not making ambient measurements. As a result we only compare model results from the 30th.
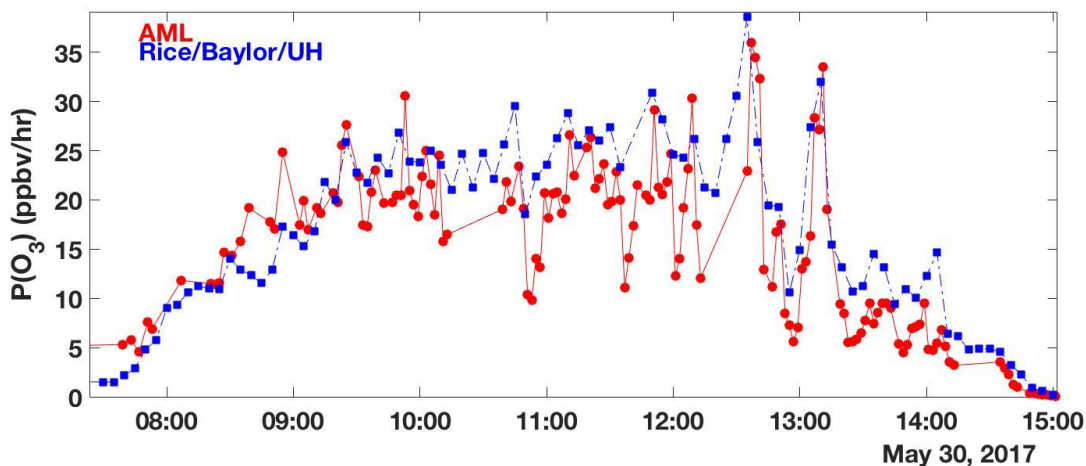
Figure 15. Time series of modeled $P(O_3)$ using the GEOSChem mechanism at the UTSA site on May 30th using observations from the AML (red) and from BU/UH (blue).

There was excellent agreement between modeled $P(O_3)$ with the two observational datasets, with median values of 16.8 ppbv/hr and 16.4 ppbv/hr for the AML and BU/UH observations, respectively (Figure 15). BU/UH observations are slightly higher as compared to the AML output. Differences likely result from the accumulated differences in observations as most constrained species differ on the order of 5-10% between the two datasets. Because HCHO differed the most between the AML and BU/UH and because accurate HCHO constraints are necessary to model XO_2 and $P(O_3)$ correctly, we performed an additional model run in which we replaced the BU/UH HCHO with that from the AML. Resultant $P(O_3)$ differed from the baseline run by less than 1% on average, suggesting that differences in the HCHO observations will not lead to large differences in modeled results.

The relationship between $P(O_3)$ and NO for the four different mechanisms is shown in Figure 16. Each mechanism shows significantly higher $P(O_3)$ than that observed at UTSA. Median $P(O_3)$ at TW was 21.3, 13.2, 10.8, and 9.3 ppbv/hr for MCMv331, GEOSChem, CB6r3, and CB05, respectively, ranging from a factor of 1.7 to 3.9 times higher than that observed at UTSA. In addition, each mechanism predicts a peak in $P(O_3)$ for all data at about 1 ppbv of NO, although the maximum of the peak varies widely among the different mechanisms. Because of the uncertainty associated with the model and measurements, we cannot definitively say which mechanism yields the "correct" $P(O_3)$ values. While $P(O_3)$ from MCMv331 is higher than other models, XO_2 and $P(O_3)$ at UTSA agreed with the observations within combined measurement and model uncertainty. If $P(O_3)$ rates at TW are as high as suggested by MCMv331, then it is likely that these rates are confined to near the surface, as O_3 concentrations downwind of downtown San Antonio would be substantially higher than those seen at TW. The vertical profile of $P(O_3)$ in the region is investigated further in Section 5. In any case, the higher $P(O_3)$ and NO at TW suggests that the instantaneous ozone production regime at TW could be different than that at UTSA.
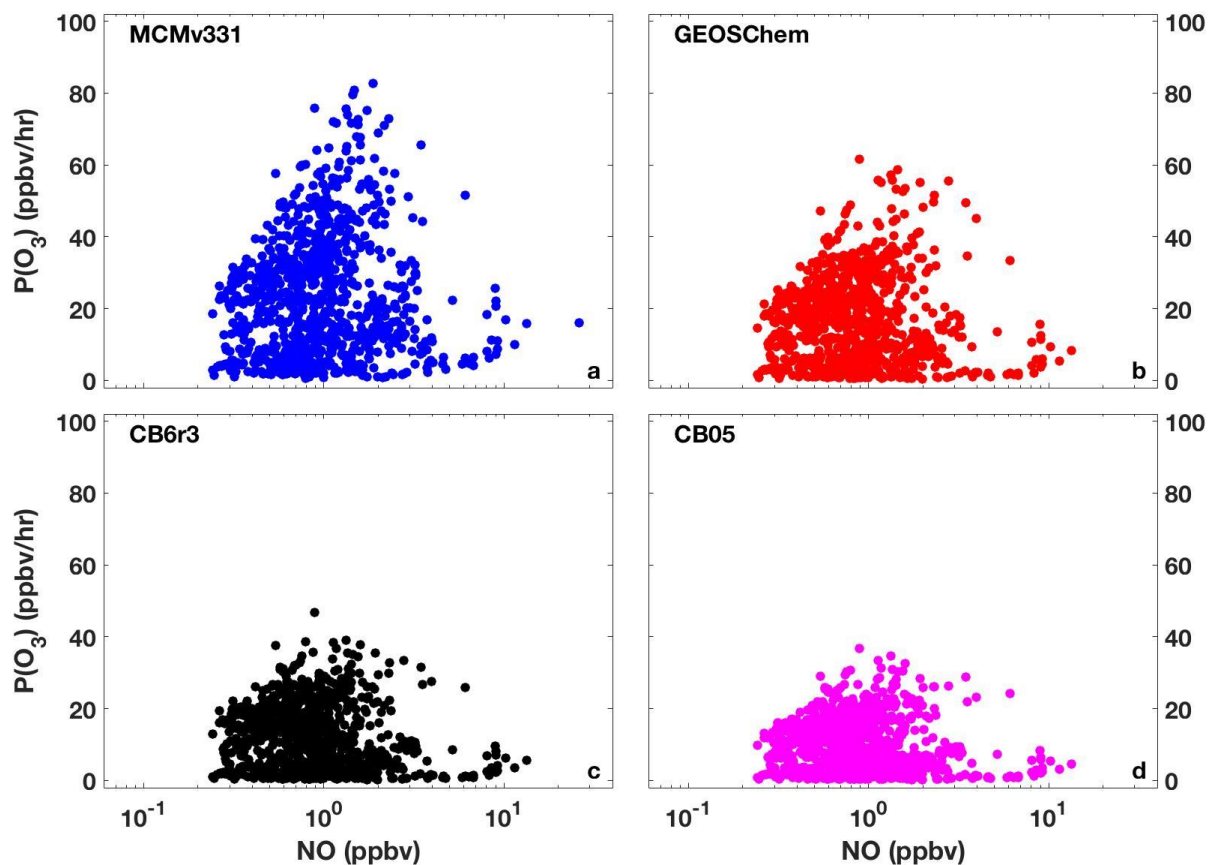
Figure 16. Modeled P(O$_3$) versus NO at TW using the MCMv331 (**a**), GEOSChem (**b**), CB6r3 (**c**), and CB05 (**d**).

To further investigate the ozone production regime at TW, we separate the modeled P(O$_3$) by P(RO$_X$) as described in Section 3. Figure 17 shows the relationship between P(O$_3$) and NO at the TW site for P(ROx) greater than 0.4 pptv/s. In addition to the results from the different chemical mechanisms, we also show the observed P(O$_3$) versus NO relationship at UTSA for comparison. As discussed earlier, P(O$_3$) at UTSA peaks at about 10 ppbv/hour at 300 pptv NO. In contrast, each mechanism shows a clear increase in P(O$_3$) up to about 1.8 ppbv at TW, peaking between 30 ppbv/hr for CB05 and 65 ppbv/hr for MCMv331. For GEOSChem, CB6r3, and CB05, there is also a clear decrease in P(O$_3$) after the peak, likely indicating a transition from the NO$_X$- to VOC-limited regime, assuming the VOC reactivity is not very different. Unlike at UTSA, there is significant ozone production in the VOC-limited regime, suggesting that reductions in NO$_X$ emissions could lead to increased instantaneous ozone production rates in downtown San Antonio at the surface, though the overall effect of NOx emission reductions on ozone concentrations of course depends on ozone production rates over a large geographic area (both horizontally and vertically).
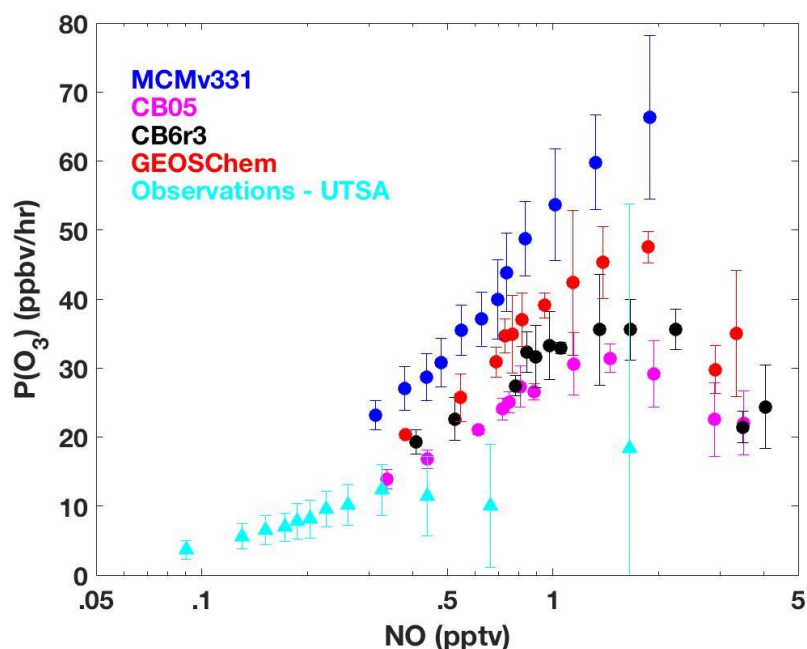
Figure 17. Relationship between P(O₃) and NO for the four chemical mechanisms at TW. Only showing results for points where $P(RO_X) > 0.4$ pptv/s. Data are mean values for NO bins with an equal number of observations in each bin. Error bars represent one standard deviation. In addition, the observations from the UTSA site are shown for comparison.

The contributors to P(O₃) at TW are shown in Figure 18. Whereas P(O₃) peaked at 10 or 11 am at UTSA, each mechanism shows a clear peak in P(O₃) at 13:00. Similar to UTSA, the predominant contributors to ozone production are HO₂ and isoprene. For isoprene, at 13:00, when P(O₃) peaks, the contribution from isoprene for both MCMv331 and GEOSChem was 5.6 ppbv/hr, or 13% and 21% of total P(O₃) respectively. The magnitude is slightly lower for CB6r3 at 3.2 ppbv/hr. Production rates from HO₂ range from 13.4 for CB05 to 17.9 ppbv/hr for MCMv331. Unlike at UTSA, MCMv331 shows that alkanes are responsible for at least 6% of total P(O₃), while alkanes are responsible for only 3% of total P(O₃) in GEOSChem. For the MCMv331, the contribution from alkanes is likely higher because several species in the other category can be derived from both alkanes and alkenes. As before, the main driver of differences between MCMv331 and GEOSChem and CB6r3 is the other category, which in this case includes contributions from alkenes.
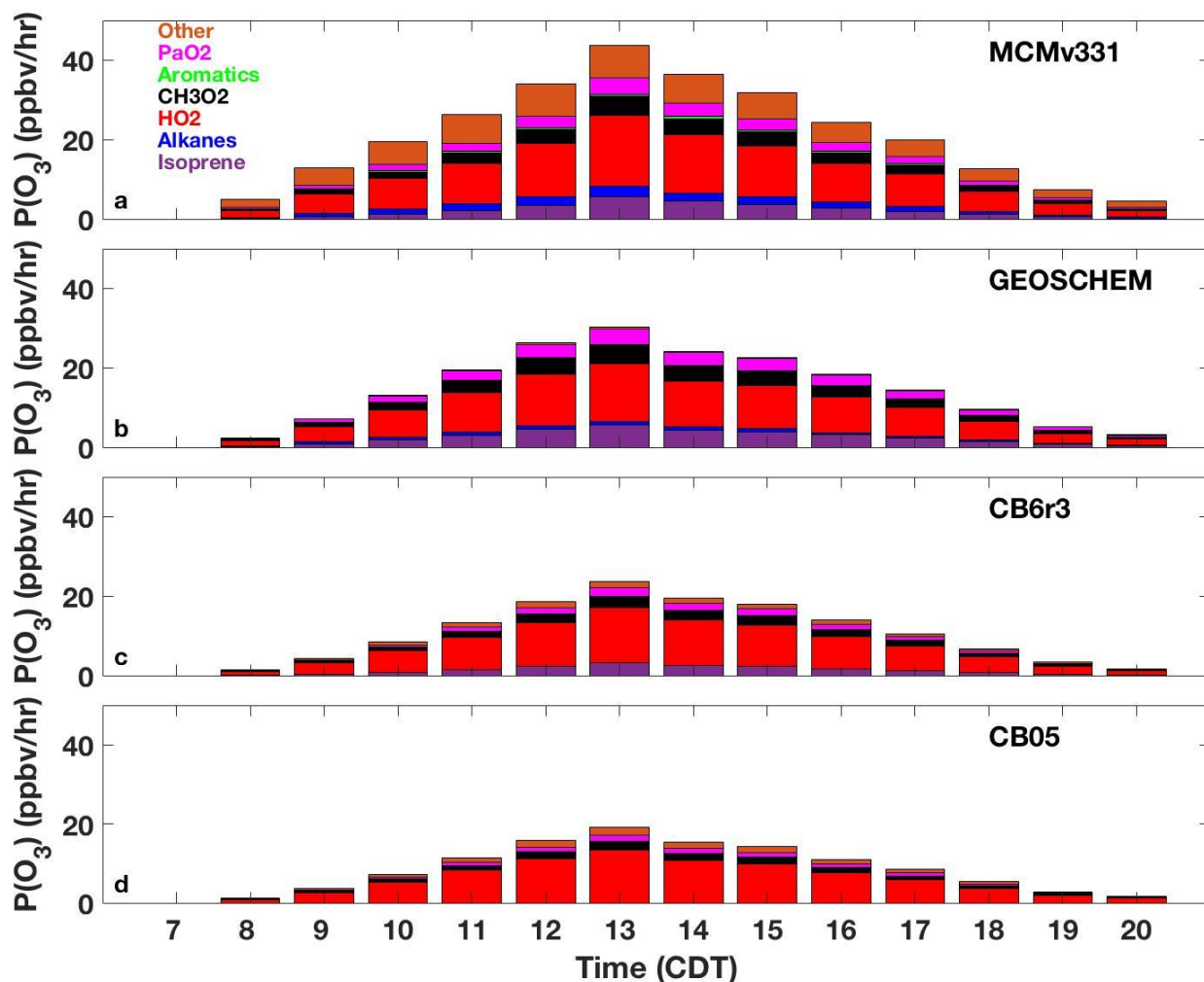
Figure 18. Same as Figure 14 except at UTSA.

5. Task 3

Apportion O₃ concentrations to location-specific emission source using 3-D air quality modeling with the instrumented Community Multiscale Air Quality model (CMAQ)

5.1 Model field campaign episode

While Tasks 1 and 2 leveraged data from the SAFS field campaign to relate P(O₃) to NOx in the greater San Antonio area, Task 3 used 3-D chemical transport modeling to assess the influence of select emissions sources on ozone in San Antonio, specifically, and Texas, more broadly. The Community Multiscale Air Quality (CMAQ) model was used to model an episode during May 2017 corresponding to the field campaign.

The modeling platform was supplied by Kirk Baker, a Physical Scientist in the Office of Air Quality Planning and Standards (OAQPS) at the U.S. Environmental Protection Agency (EPA). The model resolution was 12-km by 12-km horizontally with 35 vertical layers up to 50 mbar The chemical mechanism was the fourth version of Carbon Bond 6 (CMAQ option: CB6r3) (Yarwood et al., 2010; Emery et al., 2015) for treatment of gas phase reactions, which was also

29

used in Task 2 0-D box modeling. The aqueous chemistry mechanism as well as aerosol dynamics and thermodynamics were represented with the most recent treatment (CMAQ option: aero6). Additionally, primary organic aerosol were treated with the potential to be semivolatile and age in the gas phase (Murphy et al., 2017) (CMAQ option: nvPOA). Meteorology was driven by results from the Weather Research and Forecasting model. Emissions included the 2017 National Emissions Inventory as well as biogenic emissions as modeled by BEIS v.3.6.1. These were preprocessed by OAQPS with the Sparse Matrix Operator Kernel Emissions (SMOKE) model for use in CMAQ. The model was run on a local high performance computing (HPC) system, Proteus, which is the shared condominium HPC system with 2496 compute cores. Proteus runs at a peak speed of 25 TFLOPS and provides 9.5 TB of RAM. The modeling platform was run with CMAQ v.5.2.1, which was readily available when the modeling platform was provided by Kirk Baker in February 2019. This model was the same version used by OAQPS when they created these inputs.

5.2 Model evaluation
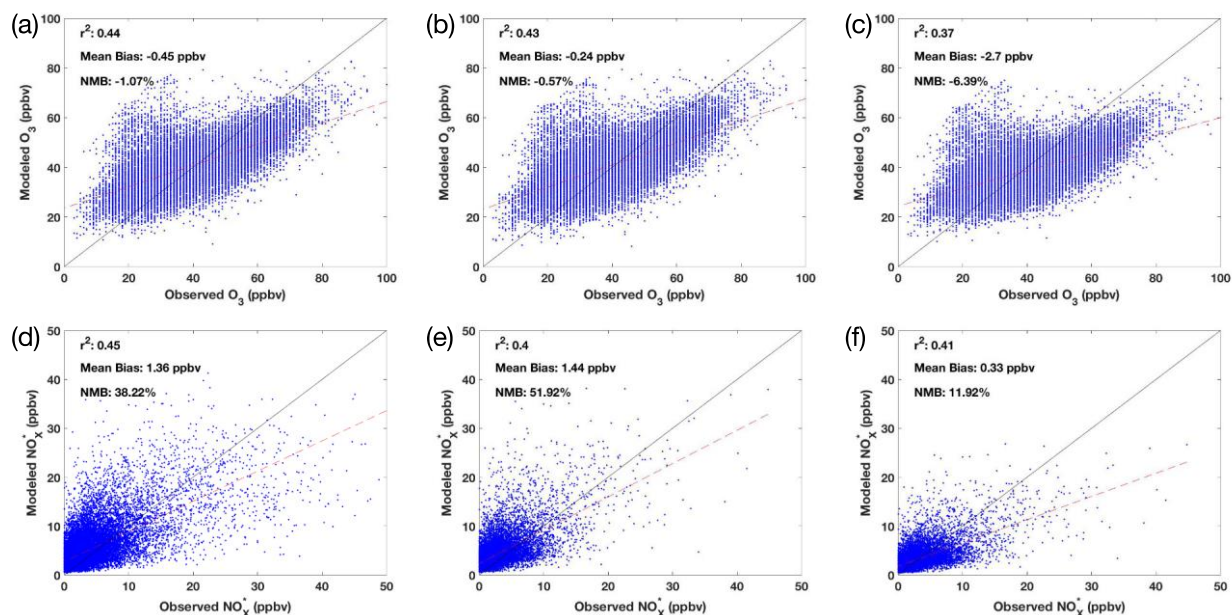
Figure 19. Comparisons of Texas AQS hourly average measurements of O_3 to (**a**) CMAQ v.5.2.1 baseline, (**b**) CMAQ v.5.3β baseline, and (**c**) CMAQ v.5.3β 30% NOx area source emissions reduction domain-wide to hourly average modeled O_3 collocated in time and space. Comparisons of PAMS hourly average measurements of observed hourly average NOx* from non-roadside monitors to spatially and temporally collocated modeled hourly average NOx with (**d**) CMAQ v.5.2.1 baseline, (**e**) CMAQ v.5.3β baseline, and (**f**) CMAQ v.5.3β 30% NOx area source emissions reduction domain-wide.

The model results were evaluated against observations included in EPA's Air Quality System (AQS). Specifically, the hourly O_3 in a model grid cell collocated with a measurement site was compared to the temporally aligned measurements throughout May 2017 for Texas AQS sites. Additionally, the modeled hourly average nitrogen oxide concentrations were compared to the

temporally aligned and spatially collocated measurements from Photochemical Assessment Monitoring Stations (PAMS) not located at a roadside in Texas for the same period (Figure 19c-e). The standard measurement technique for nitrogen oxides (chemiluminescence, with catalytic conversion of higher nitrogen oxides to NO on heated molybdenum) is not completely selective for NO_2 and subject to interferences from organic nitrates and some fraction of nitric acid [*Dickerson et al.*, 2019]. We therefore compare the observed nitrogen oxides to modeled NO_X^*, which we define as the sum of NO_X, organic nitrates, and PANs. The O_3 mean bias and normalized mean bias (NMB) for ozone were well within the bounds of reasonable model performance at -0.45 ppbv and -1.07%, respectively. The correlation was negatively impacted by the overprediction of some O_3 concentrations less than 40 ppbv. The performance of NOx^* was slightly worse in terms of mean bias (1.36 ppbv), but because the mean is small, the NMB is 38.22%. Accordingly, room for improvement exists in the modeled NOx^* in this episode and region.

In addition to the comprehensive assessment across the month, we analyzed daily spatial patterns of O_3 and identified an overestimation arising from transport from the southern boundary conditions. The boundary conditions provided by Kirk Baker were from the near-real time hemispheric modeling conducted by EPA's Office of Research and Development (ORD). These boundary conditions transported ozone into Texas from Mexico that did not appear in the monitored values. The source may, in part, be from wildfires, which were modeled with the FINN inventory outside the U.S. and the SmartFire2/BlueSky algorithm within the U.S. To ensure that the issue was not associated with wildfire within the modeling domain, a sensitivity run with CMAQ v.5.2.1 was conducted in which point source fire emissions from the U.S. were turned off. The resulting ozone changes were within the limits of numerical noise. We provided this feedback to OAQPS who confirmed that the same overestimation was observed in a separate modeling platform that Barron Henderson was using with different boundary conditions. In each, O_3 was overestimated during May from the southern boundary of the continental U.S. To date, this issue has not been resolved.

5.3 Sensitivity analysis with emissions

With reasonable comparisons of ground-based observations and modeled O_3 and NOx^*, we sought to identify emissions sources influential in O_3 formation near San Antonio. Ben Murphy of EPA's ORD provided a beta version of CMAQ v.5.3 (CMAQ v.5.3β) in which he has implemented a new framework for scaling emissions within CMAQ. Although this code is not yet publicly available, the release of CMAQ v.5.3 scheduled for late summer 2019 is slated to include this addition. The model was configured with the same options as CMAQ v.5.2.1, which required very minor corrections to the code we received. This framework enables the multiplicative scaling of selected species from emissions sources that are represented in unique input files. Spatial masks define the region across which the emissions perturbation is applied. CMAQ-ISAM development has been delayed compared to the timeline expected last year on account of a transition of developers within EPA; therefore, the remainder of the work leverages the emissions scaling factors for sensitivity analysis.

To evaluate the influence of select regional emissions sources on O_3 in San Antonio and Texas, the same modeling approach was taken with CMAQ v.5.3β followed by sensitivity analysis runs. First, the CMAQ v.5.3β baseline case was run with the same chemical mechanism settings as CMAQ v.5.2.1. The model performance for O_3 and NOx[*] was comparable to CMAQ v.5.2.1 with slight improvement in O_3 and moderate degradation of NOx[*] performance (Figure 19a,b,d,e). Satisfied that the CMAQ v.5.3β model was behaving as designed, we executed four modeling scenarios with adjusted emissions of select species from selected areas and sources (Table 2). Given the positive normalized mean bias for NOx[*], we posited that a reduction in area NOx emissions may improve model performance. Although the 2017 NEI has not been evaluated by other modeling groups, *Souri et al.* [2016] showed that a 30% reduction in the 2011 NEI area NOx emissions improved model agreement with observations made during the DISCOVER-AQ campaign in Houston. When we implemented a 30% reduction in area NOx emissions in Texas, modeled NOx[*] compared more favorably with observed concentrations from monitors not by roadsides than had the baseline case with an NMB of 11.92% (Figure 19d,e). Therefore, we considered this case to better represent reality than the baseline case. Accordingly, sensitivity analysis cases include a simulated 20% reduction in NOx (represented by a 50% reduction in area sources) as well as 100% reductions of electricity generating unit (EGU) in Texas outside of San Antonio and oil and gas point sources in Texas outside of San Antonio in which the 30% reduction of Texas area sources of NOx was maintained.

Table 2. Sensitivity analysis runs with CMAQ v.5.3β.

Name	Species	Region	Source	Reduction
30NOx	NO, NO₂	Domain	area sources	30%
50NOx	NO, NO₂	Domain	area sources	50%
zeroEGU	all | NO, NO₂	Texas except San Antonio	EGU point sources | area sources	100% | 30%
zeroOil	all | NO, NO₂	Texas except San Antonio	oil & gas point sources | area sources	100% | 30%

The spatial patterns of monthly average surface O_3 show that the 30NOx case made the most substantial differences across the state (Figure 20). The spatial patterns of differences between the 30NOx case and the baseline case from 07:00 to 19:00 averaged over the month show that the ozone reductions were widespread (Figure 21a). Larger cities in Texas had smaller reductions, but only two locations in Mexico had sufficiently high NOx concentrations to induce titration of ozone that resulted in increases when the 30% area reduction was applied. For the other sensitivity analysis cases, the differences are shown from the 30NOx case given that this case better represented the observed NOx[*]. Again, the area source NOx emissions reduction by an additional 20% caused the greatest difference in ozone (Figure 21b). On average in this half of the domain, the differences from EGU exceed those of oil and gas point sources though both are small (Figure 21c,d).
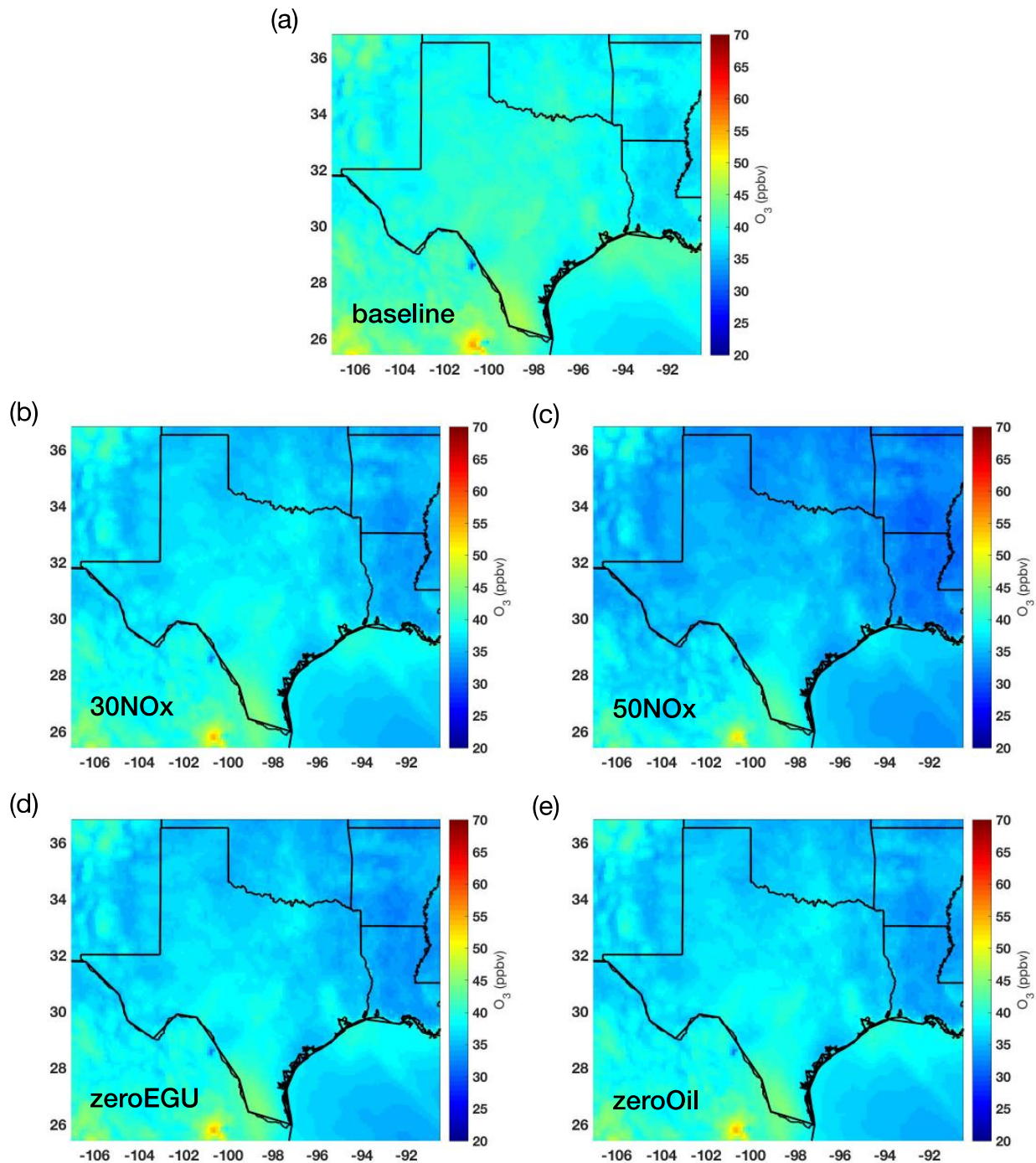
Figure 20. The spatial patterns of monthly average surface O_3 in May 2017 for the CMAQ v.5.3β (**a**) baseline case, (**b**) 30% NOx area source emissions domain-wide reduction case, (**c**) 50% NOx area source emissions domain-wide reduction case, (**d**) 100% reduction in Texas EGU point source emissions with 30% NOx area source emissions domain-wide reduction case, and (**e**) the 100% reduction in Texas oil and gas point source emissions with 30% NOx area source emissions domain-wide reduction case.
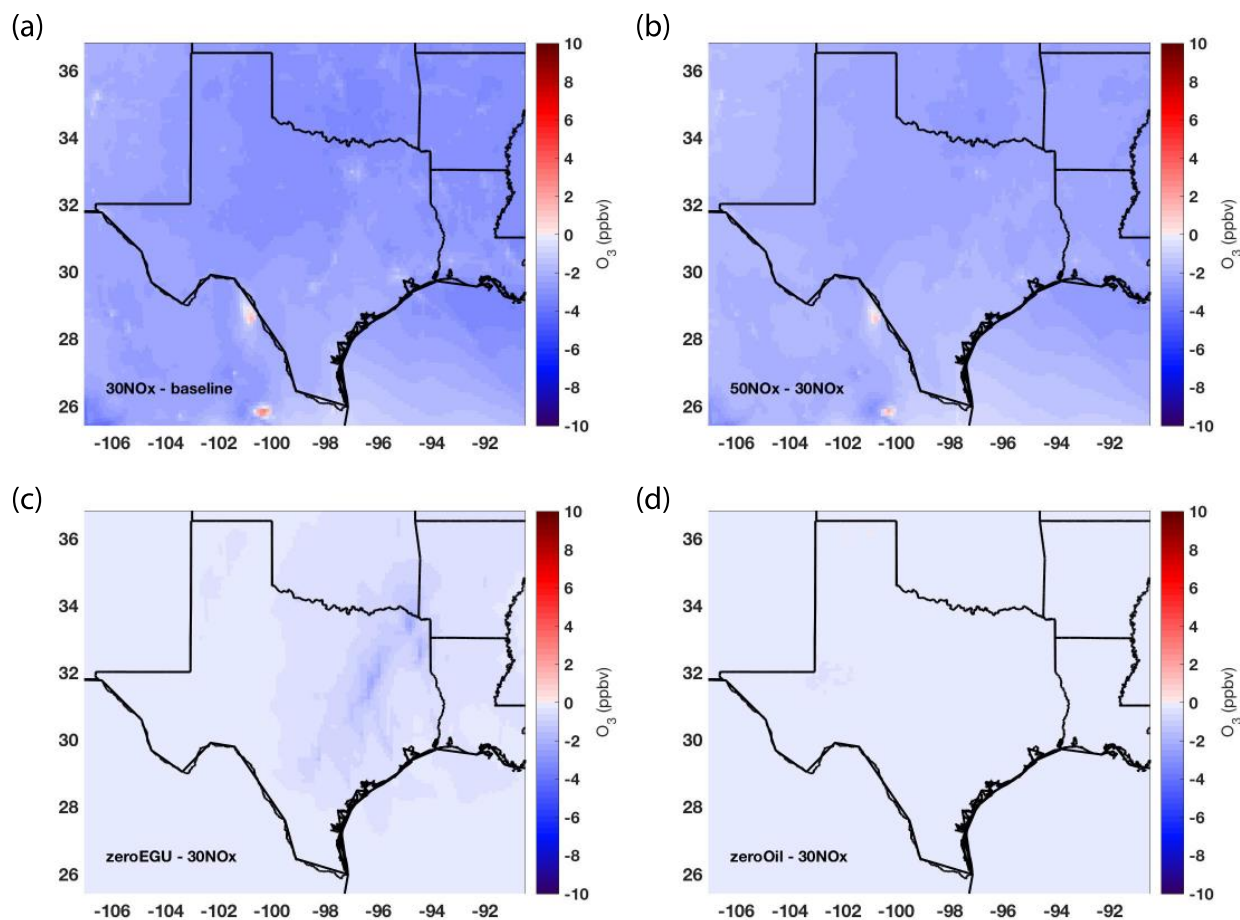
Figure 21. The spatial patterns of monthly average ozone differences during 07:00-19:00 in May 2017 (**a**) from the CMAQ v.5.3β baseline case for 30% NOx area source emissions domain-wide reduction (30NOx) case. The same spatial patterns but the difference from the 30NOx case of the (**b**) 50% NOx area source emissions domain-wide reduction case (50NOx), (**c**) 100% reduction in Texas EGU point source emissions with 30% NOx area source emissions domain-wide reduction case (zeroEGU), and (d) the 100% reduction in Texas oil and gas point source emissions with 30% NOx area source emissions domain-wide reduction case (zeroOil).

Nevertheless, the temporal average obscures the day-to-day variability of these 07:00 – 19:00 differences, which is not negligible in San Antonio (Figure 22). Hourly O_3 in the 30NOx case is more than 5 ppbv lower than the baseline case at the point of greatest difference but is larger by almost 2 ppbv at the upper extreme. The median difference is nearly 2 ppbv. For the 50NOx case, the median additional reductions from the 30NOx case are just shy of those obtained with the 30% area NOx reduction. The 50NOx case does not exceed the 30NOx case. For the zeroEGU case, the greatest additional reduction is slightly more than 3 ppb with some potential for a slight increase over the 30NOx ozone levels. The median is only slightly less than zero indicating a fairly small impact typically. One limitation of this approach is that plume-in-grid was not applied. For the influences of nearby or upwind power plants, this approximation should be relatively benign for the assessment of influences in San Antonio because of the dispersion of pollutants by the time they reach this location. The Lake Calaveras plants are within the San

Antonio region mask, which is excluded from the 100% reduction; therefore, the same approximations are inherent in all of the runs due to the plume-in-grid approach not being applied. Finally, the greatest impact of eliminating the oil and gas point source emissions is only a reduction of 0.5 ppbv.
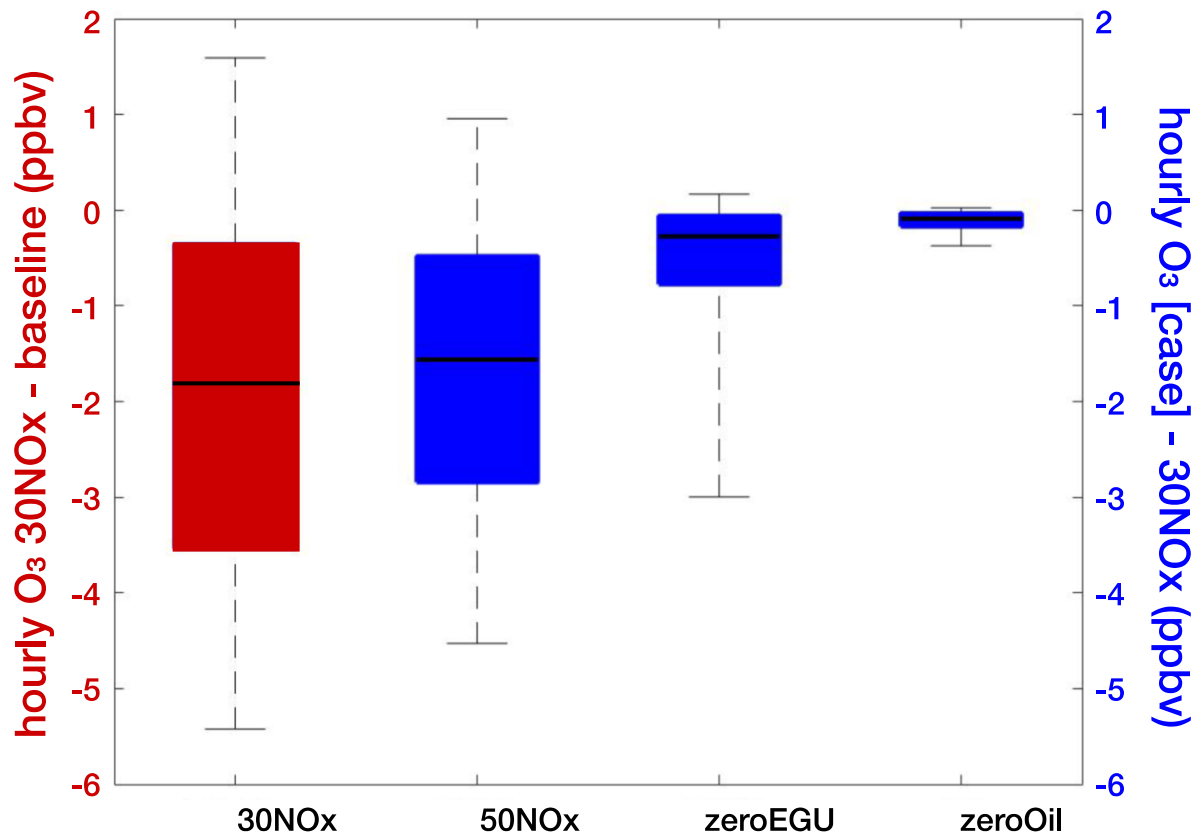
Figure 22. The distribution of the hourly average O_3 differences of modeled ozone between 07:00 and 19:00 over San Antonio for the 30NOx case from the baseline case (left, red axis) and for each sensitivity analysis case from the 30NOx case (right, blue axis) as indicated by the 5th percentile (bottom bar), 25th percentile (bottom edge of box), median (bar within box), 75th percentile (top edge of box), and 95th percentile (topmost bar). The 30NOx run is indicated as red because it shows the difference between the 30% NOx reduction and the baseline run whereas the others each show the difference between the other sensitivity analysis cases and the 30% NOx reduction case.

Eulerian chemical transport modeling affords the opportunity to explore the vertical distribution of P(O₃) and P(ROx), which is difficult to accomplish apart from flying transects through the boundary layer with instruments similar to those employed in Task 1. Instead, this approach combined hourly modeled vertical distributions of reactive VOC species throughout the lower troposphere with the reactivity information for CB6r3 used in Task 2 to calculate vertically and temporally resolved P(O₃) (Figure 23a). The surface P(O₃) is greatest throughout the day with the most substantial differentiation from P(O₃) within the mixing layer in the late afternoon hours locally (15:00 – 18:00). The import of this finding is that, as in Task 1, surface observations are used to infer P(O₃) (Figure 4), which is often extrapolated to the rate for the entire mixing layer. This analysis suggests that high P(O₃) rates near the surface, such as those seen at the Travelers' World site, might be confined to the surface, and are not necessarily representative of the rates seen throughout the mixed layer. Additionally, the vertical P(ROx) profile is shown in Figure 24b, allowing for a comparison to the measurement-based derivations from Task 1 (Figure 4). These radicals are strongly dependent on sunlight, which leads to the nearly sinusoidal shape of the production rate curve with time in each layer. In contrast with P(O₃), according to CMAQ, P(RO$_X$) is more constant throughout the mixed layer, suggesting that surface values are representative of the layer.

Finally, the modeled P(O₃) and P(ROx) can be sampled in a manner comparable to measurements to assess the extent to which the chemical mechanism represents ambient behavior. The surface P(O₃) over San Antonio for May 2017 between 07:00 and 19:00 is plotted as a function of the hourly average NO in a manner similar to that applied to measurement-based values in Task 1 (Figure 24a). The overall shape of the curve is similar, with a large increase in P(O₃) with NO for higher P(RO$_X$).
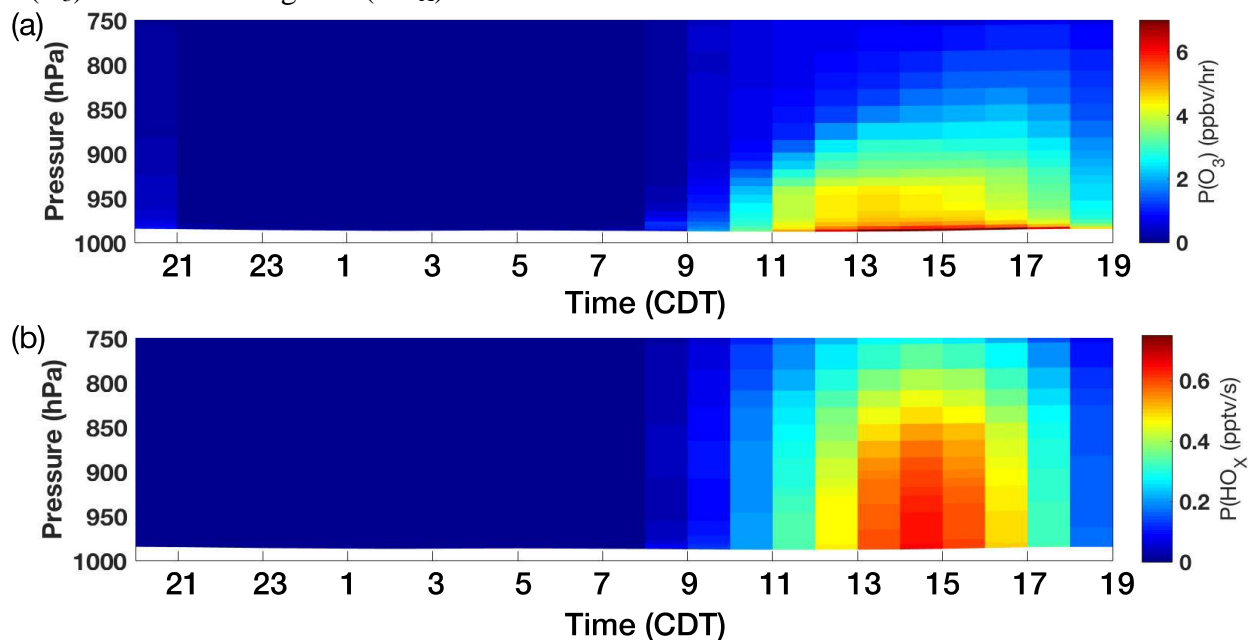

Figure 23. Vertical profiles of (**a**) P(O₃) and (**b**) P(HOx) from the 30NOx case averaged over San Antonio.
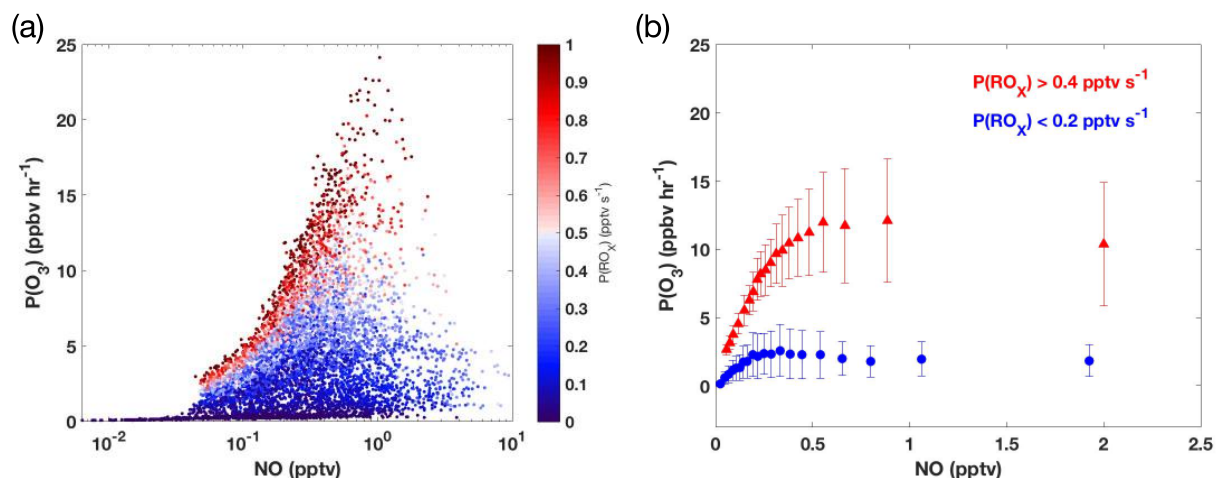
Figure 24. The variation of P(O₃) in San Antonio from 07:00 to 19:00 during May 2017 with NO. (**a**) Modeled hourly P(O₃) from the 30NOx case plotted against the modeled hourly NO colored by P(RO$_x$). (**b**) The same values are shown segregated into P(ROx) > 0.4 pptv s^{-1} (red) and P(ROx) < 0.2 pptv s^{-1} (blue) then binned by NO bins with equal numbers of modeled values per bin. The mean value of each bin is shown, with the error bars showing one standard deviation.

When the same data are binned by NO concentration, the curve of P(RO$_X$) < 0.2 pptv s^{-1} peaks near 0.3 pptv NO and then declines slightly more than observed in reality though the number of observations at higher NO levels makes it difficult to assess. Similarly, with values of P(RO$_X$) > 0.4 pptv s^{-1}, the small number of modeled, higher NO values makes it difficult to assess how much the chemical mechanism in this scenario captures the expected reduction in P(O₃) with higher NO.

6. Audits of Data Quality

Data used in Task 1 had been quality assured prior to this work being conducted.

Each version of CMAQ was first tested with the benchmark episode distributed with the model. This shorter episode on a smaller domain provided the opportunity to assess the performance of CMAQ v.5.3β against that of the publicly available CMAQ v.5.2.1. Emitted species NO₂, NO, and formaldehyde (Figure 25a,b,c) compare excellently between the two. The radical species HO₂ and OH were slightly higher in CMAQ v.5.3β than in v.5.2.1 (Figure 25d,e). The buffered species O₃ was very similar between the two model versions (Figure 25f). These results provided confidence that CMAQ v.5.3β would provide reliable predicted concentrations.
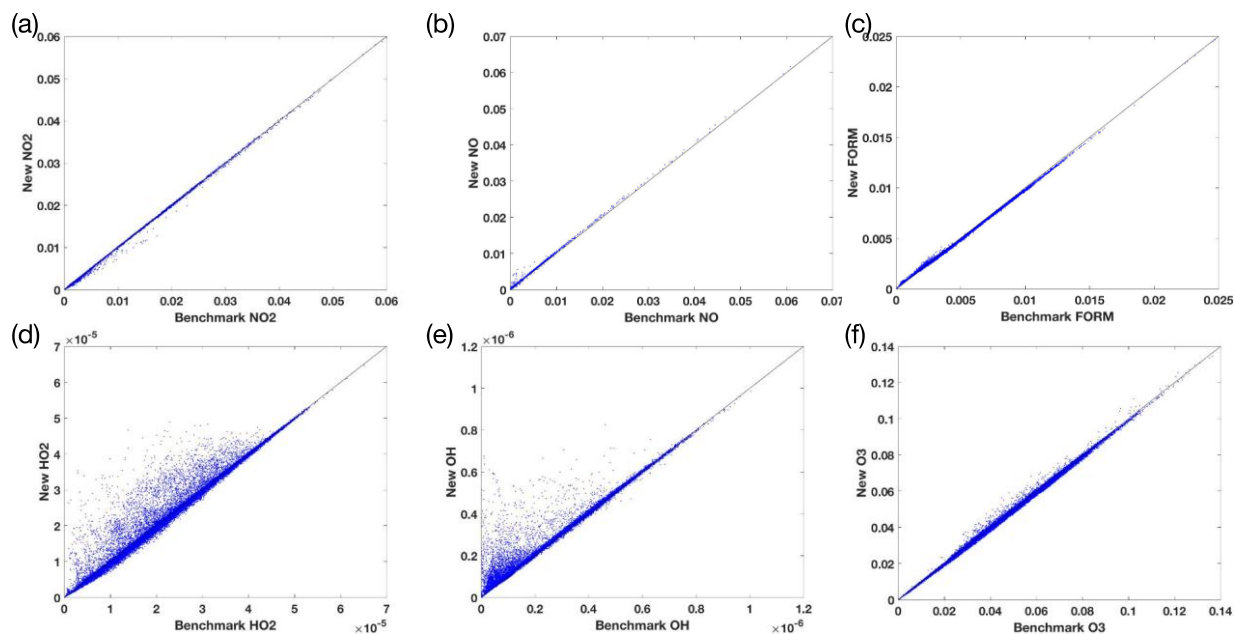
Figure 25. Comparison of hourly average concentrations of (**a**) NO$_2$, (**b**) NO, (**c**) HO$_2$, (**d**) O$_3$, (**e**) formaldehyde, and (**f**) OH from CMAQ v.5.3β against v.5.2 for the benchmark episode provided with the model.

The quality assurance of O$_3$ and oxides of nitrogen concentrations for the May 2017 episodes was discussed in Section 5.2. For all of the evaluated O$_3$ normalized mean biases were well within the 15% guideline for reasonable performance. In addition, the modeled NO$_2$ fields were compared with satellite-based observations of NO$_2$ columns from the Ozone Monitoring Instrument (OMI) with the Goddard Space Flight Center algorithm (Figure 20a). CMAQ v.5.2.1 NO$_2$ fields were processed as though OMI had flown over the modeled atmosphere and the GSFC algorithm had been used to interpret the columns while applying the same filters for clouds and other factors that inhibit retrievals (Figure 26b). See *Ring et al.* [2018] for a complete
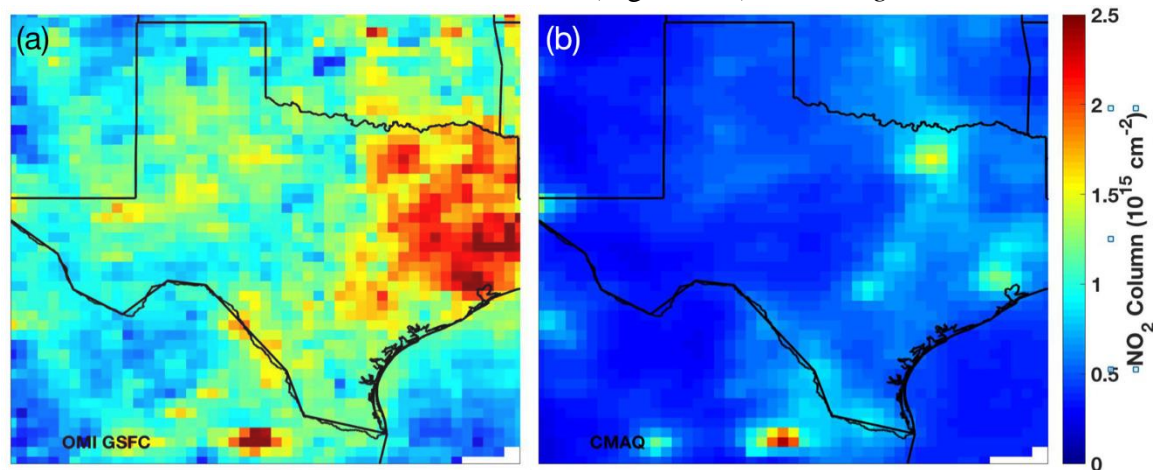
Figure 26. (**a**) The monthly average OMI GSFC NO$_2$ columns for May 2017. (**b**) The monthly average CMAQ NO$_2$ field as OMI GSFC would have interpreted them.

description of the methodology employed here. The code for processing and plotting the OMI data was verified with GIOVANNI images of the GSFC retrieval of OMI from the same time period. The monthly average NO_2 column fields both reflect higher column concentrations in major urban areas but differ in magnitude. Additionally, CMAQ seems to have lower column concentrations in rural areas than OMI, consistent with previous studies [*Canty et al.*, 2015]. Because of the large differences in the modeled columns and satellite-based observations, ground-based observations were relied upon instead for evaluating model performance and sensitivity runs.

Finally, quality assurance testing on the benchmark episode was conducted before using the new emissions scaling framework provided by Ben Murphy of EPA's ORD. The base case NO concentrations were compared to those resulting from a 50% reduction in NOx area emissions domain-wide (Figure 27a-d). In locations that appear to be dominated by mobile NOx emissions, the spatial percent differences are approximately 50% (Figure 27c), which contributes to the line with a slope of approximately 0.5 when the concentrations are plotted against one another (Figure 27d). Some points have different degrees of change because of the contributions of NO from other sources including fire, EGUs, and boundary conditions. This test confirmed that the percent scaling of emissions from a selected file was working properly.

In addition, the capability to refine emissions in a specified region was verified using the benchmark episode. To do so, area NOx emissions from one half of the domain were eliminated. The plotted percent difference shows that the top half of the domain remained unchanged while the bottom half includes nearly complete elimination of NO with the exception of what comes from the boundary conditions (Figure 27e). The bifurcation of the population when plotted against one another is evident with lines of slopes one and zero (Figure 27f).
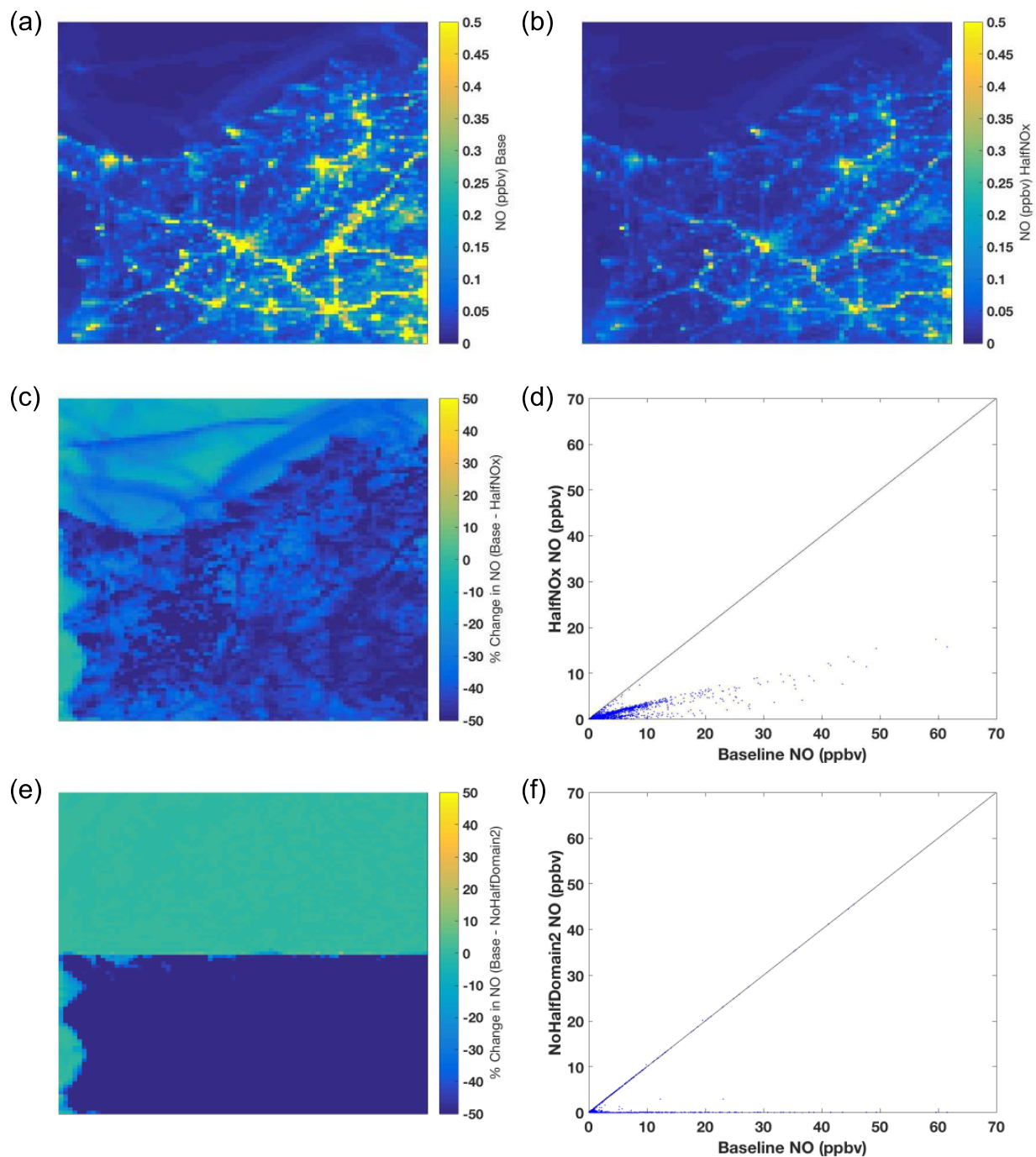
Figure 27. Benchmark testing of the CMAQ v.5.3β emissions scaling framework. (**a**) The base case benchmark NO surface concentration (ppbv). (**b**) The concentration and (**c**) percent difference when a 50% domain-wide reduction in area NOx emissions was implemented. (**d**) The comparison of NO concentrations when a 50% domain-wide reduction in area NOx emissions was implemented. (**e**) The percent difference and (**f**) comparison with the base case when a 100% reduction in area NOx emissions was implemented in only one half of the domain.

7. Conclusions and Recommendations for Future Work

Here, we have used observations made during May 2017 from the San Antonio Field Study to address three broad tasks:

1. Quantify the dependence of the ozone production rate on the concentrations of NOx, VOCs, and other measurements at the three SAFS sites where peroxy radical concentrations were measured.
2. Conduct zero-dimensional (0-D) photochemical modeling constrained by the SAFS datasets with several model chemical mechanisms for four SAFS measurement sites, spanning a large range of NOx values.
3. Apportion ozone concentrations to location-specific emission sources using 3-D air quality modeling with the instrumented Community Multiscale Air Quality model (CMAQ).

Using *in situ* observations made onboard the Aerodyne Mobile Laboratory, we have shown that ozone formation at the UTSA, Floresville, and Lake Corpus Christi sites was usually under 15 ppb/hr. Multiple lines of evidence show that UTSA was usually NOx-limited except for time periods when primary HOx radical production was low, typically in the morning or because of overcast conditions. Ozone production during these periods was typically less than 5 ppbv/hr. In contrast with cities like Houston, OH reactivity at both UTSA and Floresville was dominated by biogenic VOCs, with isoprene sometimes accounting for over 50% of total OH reactivity. Contributions from alkanes, alkenes, and aromatics were 1% or less at the UTSA site. Using *in situ* markers for biomass burning, we also attempted to determine the impact of long-range transport of biomass burning emissions on ozone production in the region. While biomass burning plumes were clearly sampled, there is little evidence from the *in situ* observations that ozone production in these plumes was enhanced when compared to air not influenced by burning emissions.

In combination with the F0AM box model, two versions of the carbon bond mechanism (CB6r3 and CB05) and the GEOS-Chem mechanism produced peroxy radical concentrations that agreed within 5% of observations. Interestingly, the master chemical mechanism (MCM 3.3.1), which is the most up-to-date and explicit mechanism, overestimated observed peroxy radicals by 27%. Each mechanism was able to reproduce the general observed relationship between ozone production and NO. Ozone production rates at the Travelers' World site, as calculated by the box model, were significantly higher than at UTSA, peaking between 40 and 80 ppbv/hr, depending on the mechanism. Median NO was more than a factor of two higher at TW, as well. CB6r2, CB05, and GEOS-Chem each suggest possible ozone production in the VOC-limited regime on the order of 20 – 30 ppbv/hr. The dominant peroxy radicals for ozone production at both UTSA and Travelers' World, according to MCM 3.3.1, CB6r3, and GEOS-Chem are HO_2 and radicals derived from isoprene, although isoprene plays a more dominant role at UTSA. Peroxy radicals from alkanes comprised a larger fraction of ozone production at Travelers' World, but still less than half that of isoprene.

Finally, to compliment the *in situ* analysis and zero dimensional modeling, we also used the CMAQ model to help determine the relative impact of different emission sectors on surface

ozone in San Antonio. Consistent with previous studies, NO_X emissions were found to be too high, overestimating concentrations at surface monitors by approximately 50%. Reducing these emissions by 30%, brought modeled NO_X to within about 10% of observations. Reducing NO_X emissions by a further 20% lead to median reductions in surface ozone in San Antonio of 2 ppbv over May 2017. Emissions from power plants outside of San Antonio only produced a median of 0.25 ppbv ozone at the surface, although there was significant daily variation, with contributions up to 3 ppbv. Emissions from oil and gas operations seem to have minimal impact on San Antonio ozone. The relationship between surface ozone production and NO for high primary HO_X production was similar between CMAQ and observations, with maximum values of about 15 ppbv. Vertical profiles of ozone production show that the highest ozone production rates are limited to near the surface.

Additional research into the sources of ozone production in San Antonio is still needed. While the *in situ* observations did not show any significant influence of biomass burning on ozone production, those results were limited to two sites that were also influenced by factors that could mask the impact of biomass burning. There were significant fires on the Yucatan peninsula during SAFS, a location that was outside of the modeling domain used here for CMAQ and was therefore only represented through the boundary conditions. An investigation into the impact of those boundary conditions on modeled surface ozone is warranted to determine the effects of not only fires but also ozone transported from outside the model domain.

Peroxy radical concentrations were not measured at the high-NOx, centrally-located Traveler's World site, and so measurement-constrained ozone production rates could not be determined there. Given that the instantaneous ozone production rates predicted by the 0-dimensional model were much higher at Traveler's World site (peak values between 30 and 65 ppb/hr depending on chemical mechanism) and the divergence of results for the various chemical mechanisms, the amount of ozone produced in central San Antonio remains fairly uncertain and worthy of follow-up research. Furthermore, the impact of biomass burning on ozone formation, if any, is likely to be most apparent at that site given that aged biomass burning smoke is typically depleted in NOx and so mixing of VOC-rich smoke with fresh, local urban NOx emissions could lead to a synergistic impact on ozone formation rates.

We have shown that reducing NO_X emissions by 20% across the model domain only leads to reductions in surface ozone in San Antonio on the order of 3 ppbv, suggesting that a large component of ozone in the San Antonio region could be from regional background values. A source apportionment study, either using ISAM when it becomes available (expected in late 2019) or a more brute force method, should be conducted to determine the relative impact of emissions from different geographic areas, such as Mexico and other US states, on ozone production.

In this study, we used the OMI instrument to investigate the ozone production regime in San Antonio. While informative, OMI suffers from data quality issues due to its age. After the field study concluded, the TROPOMI satellite was launched. This instrument provides retrievals of the same species as OMI at a higher resolution and would likely have more valid data per swath, allowing for less spatial and temporal averaging. In addition, using TROPOMI to investigate

NO$_2$ and HCHO columns as well as the ozone production regime would allow for analysis over the entire year, instead of just May, to allow for investigations into seasonal variability. While still not launched, a similar analysis could be used with the upcoming TEMPO satellite, which is designed to provide hourly retrievals for some species, allowing for the determination of diurnal variation in these values as well.

References

Anderson, D. C., et al. (2017), Formaldehyde in the Tropical Western Pacific: Chemical Sources and Sinks, Convective Transport, and Representation in CAM-Chem and the CCMI Models, *Journal of Geophysical Research-Atmospheres*, *122*(20), 11201-11226, doi:10.1002/2016jd026121.

Canty, T. P., L. Hembeck, T. P. Vinciguerra, D. C. Anderson, D. L. Goldberg, S. F. Carpenter, D. J. Allen, C. P. Loughner, R. J. Salawitch, and R. R. Dickerson (2015), Ozone and NOx chemistry in the eastern US: evaluation of CMAQ/CB05 with satellite (OMI) data, *Atmospheric Chemistry and Physics*, *15*(19), 10965-10982, doi:10.5194/acp-15-10965-2015.

Dickerson, R. R., D. C. Anderson, and X. Ren (2019), On the use of data from commercial NOx analyzers for air pollution studies, *Atmospheric Environment*, 116873, doi:https://doi.org/10.1016/j.atmosenv.2019.116873.

Jaffe, D. A., and N. L. Wigder (2012), Ozone production from wildfires: A critical review, *Atmospheric Environment*, *51*, 1-10, doi:10.1016/j.atmosenv.2011.11.063.

Jenkin, M. E., S. M. Saunders, V. Wagner, and M. J. Pilling (2003), Protocol for the development of the Master Chemical Mechanism, MCM v3 (Part B): tropospheric degradation of aromatic volatile organic compounds, *Atmospheric Chemistry and Physics*, *3*, 181-193.

Jenkin, M. E., J. C. Young, and A. R. Rickard (2015), The MCM v3.3.1 degradation scheme for isoprene, *Atmospheric Chemistry and Physics*, *15*(20), 11433-11459, doi:10.5194/acp-15-11433-2015.

Kebabian, P. L., S. C. Herndon, and A. Freedman (2005), Detection of Nitrogen Dioxide by Cavity Attenuated Phase Shift Spectroscopy, *Analytical Chemistry*, *77*(2), 724-728, doi:10.1029/.

Kebabian, P. L., E. C. Wood, S. C. Herndon, and A. Freedman (2008), A Practical Alternative to Chemiluminescence-Based Detection of Nitrogen Dioxide: Cavity Attenuated Phase Shift Spectroscopy, *Environmental Science & Technology*, *42*(16), 6040-6045.

Kleinman, L. I. (2005), The dependence of tropospheric ozone production rate on ozone precursors, *Atmos. Env.*, *39*(3), 575-586.

Marvin, M. R., et al. (2017), Impact of evolving isoprene mechanisms on simulated formaldehyde: An inter-comparison supported by in situ observations from SENEX, *Atmospheric Environment*, doi:10.1016/j.atmosenv.2017.05.049.

McManus, J. B., M. S. Zahniser, D. D. Nelson, J. H. Shorter, S. C. Herndon, D. Jervis, M. Agnese, R. McGovern, T. I. Yacovitch, and J. R. Roscioli (2015), Recent progress in laser-based trace gas instruments: performance and noise analysis, *Applied Physics B-Lasers and Optics*, *119*(1), 203-218, doi:10.1007/s00340-015-6033-0.

Orlando, J. J., and G. S. Tyndall (2012), Laboratory studies of organic peroxy radical chemistry: an overview with emphasis on recent issues of atmospheric significance, *Chemical Society Reviews*, *41*(19), 6294-6317.

Pollack, I., T. Ryerson, M. Trainer, D. Parrish, A. Andrews, E. Atlas, D. Blake, S. Brown, R. Commane, and B. Daube (2012), Airborne and ground-based observations of a weekend effect in ozone, precursors, and oxidation products in the California South Coast Air Basin, *Journal of Geophysical Research: Atmospheres*, *117*(D21).

Pollmann, J., D. Helmig, J. Hueber, D. Tanner, and P. P. Tans (2006), Evaluation of solid adsorbent materials for cryogen-free trapping - gas chromatographic analysis of atmospheric C2-C6 non-methane hydrocarbons, *Journal of Chromatography A*, *1134*(1-2), 1-15, doi:10.1016/j.chroma.2006.08.050.

Ring, A. M., T. P. Canty, D. C. Anderson, T. P. Vinciguerra, H. He, D. L. Goldberg, S. H. Ehrman, R. R. Dickerson, and R. J. Salawitch (2018), Evaluating commercial marine emissions and their role in air quality policy using observations and the CMAQ model, *Atmospheric Environment*, *173*, 96-107, doi:10.1016/j.atmosenv.2017.10.037.

Saunders, S. M., M. E. Jenkin, R. G. Derwent, and M. J. Pilling (2003), Protocol for the development of the Master Chemical Mechanism, MCM v3 (Part A): tropospheric degradation of non-aromatic volatile organic compounds, *Atmospheric Chemistry and Physics*, *3*, 161-180.

Shetter, R. E., et al. (2003), Photolysis frequency of NO2: Measurement and modeling during the International Photolysis Frequency Measurement and Modeling Intercomparison (IPMMI), *Journal of Geophysical Research-Atmospheres*, *108*(D16), doi:10.1029/2002jd002932.

Souri, A. H., Y. S. Choi, W. B. Jeon, X. S. Li, S. Pan, L. J. Diao, and D. A. Westenbarger (2016), Constraining NOx emissions using satellite NO2 measurements during 2013 DISCOVER-AQ Texas campaign, *Atmospheric Environment*, *131*, 371-381, doi:10.1016/j.atmosenv.2016.02.020.

Stark, H., B. M. Lerner, R. Schmitt, R. Jakoubek, E. J. Williams, T. B. Ryerson, D. T. Sueper, D. D. Parrish, and F. C. Fehsenfeld (2007), Atmospheric in situ measurement of nitrate radical (NO3) and other photolysis rates using spectroradiometry and filter radiometry, *Journal of Geophysical Research-Atmospheres*, *112*(D10), doi:10.1029/2006jd007578.

Volkamer, R., P. Sheehy, L. T. Molina, and M. J. Molina (2010), Oxidative capacity of the Mexico City atmosphere – Part 1: A radical source perspective, *Atmospheric Chemistry and Physics*, *10*(14), 6969-6991, doi:10.5194/acp-10-6969-2010.

Wolfe, G. M., et al. (2016a), Formaldehyde production from isoprene oxidation across NOx regimes, *Atmospheric Chemistry and Physics*, *16*(4), 2597-2610, doi:10.5194/acp-16-2597-2016.

Wolfe, G. M., M. R. Marvin, S. J. Roberts, K. R. Travis, and J. Liao (2016b), The Framework for 0-D Atmospheric Modeling (F0AM) v3.1, *Geosci. Model Dev.*, *9*(9), 3309-3319, doi:10.5194/gmd-9-3309-2016.